POLITECNICO DI TORINO

Master's Degree Course in Biomedical Engineering

Master's Degree Thesis

Numerical simulations of soft solids moving through compliant walls

Supervisor
Luca Brandt

Candidate
Fabrizio Spensieri

Co-supervisor
Kiran Satheeshchandran

March 2026

Chapter 1

Introduction

1.1 Context and motivation

The study of solid particles within confined flows is of particular interest across numerous fields, ranging from natural systems to the resulting engineering applications[9]. In the pharmaceutical domain, understanding the behavior of such particles enables their use as carriers for the transport and controlled release of drugs, or to perform screening processes for diagnostic purposes. The fundamental property is deformability, that is, how easily the particle changes shape, because it alters how stresses are distributed within the solid, how it orients itself, and ultimately how it moves within a confined space[4].

In confined flows, the ability of particles to deform becomes even more significant, since confinement amplifies small variations in the material response into larger variations of the overall response. This aspect becomes even more relevant when the boundaries delimiting the duct are themselves elastic[10, 11]. Wall rigidity is commonly taken for granted in many experimental and applicative situations, due to various factors. This is a good approximation in many real devices, where the channel thickness can be considered negligible relative to its dimensions. It ensures a lower computational cost and consequently faster and more efficient simulations, since the number of parameters used and the complexity of the problem are reduced, which can otherwise lead to instabilities and thus fail to guarantee consistency in the results[6].

However, accounting for wall deformability becomes necessary in many other contexts, where one aims to study behavior as realistically as possible. In the cardiovascular field this assumption is fundamental, because many quantities used to interpret, localize, and estimate the risk of pathologies are sensitive to the dependence that arises between vessel mechanics and the internal fluid dynamics[13]. Wall stresses are often indicators of the progression of pathologies such as atherosclerosis or ischemic events[5]. This is no longer merely a matter of numerical and model refinement; rather, it increases the reliability of estimates under physiological conditions by reducing the discrepancy between simulation and expected response, thereby enabling a reliable assessment in clinically relevant scenarios[13].

It is important to understand how the presence of dual compliance influences transport processes compared with the case in which confinement is considered rigid. In a coupled system, the wall is no longer simply a geometric constraint, but will also play a role in the dynamics, because its deformation will locally modify the shape of the velocity field and, even more importantly, will also reorganize the pressure and stress fields in regions near the boundary[9, 10]. This could potentially lead to the development of forces acting transversely to the flow direction due to the way confinement is deformed, influencing the lateral motion of the

particle and significantly affecting its trajectory, its orientation, and the final equilibrium at rest within the duct.

In this thesis, the physical problem of interest is the passage of a deformable solid particle through a pressure-driven constricted channel with compliant walls. The analysis focuses on how particle deformability and wall deformability jointly influence transport, shape evolution, and downstream recovery in a confined configuration.

1.2 State of the art

The state of the art that follows outlines the main numerical approaches used to study fluid–structure interactions in the presence of deformable solid particles, focusing on the formulations adopted in the literature, their strengths, their limitations, and the associated trade-offs. Attention is placed on fully Eulerian methods (or Eulerian–Lagrangian hybrid ones), on mass and volume conservation, on stability over long simulation times and, finally, on the consistency between the interface and deformation fields, evaluating criteria such as the ability to maintain an accurate representation, mass and volume conservation over long times, and robustness in the vicinity of the walls.

From a computational standpoint, the dynamics of solids within confined flows has been analyzed mainly through Lagrangian or Eulerian–Lagrangian hybrid methods. This applies primarily to capsules, in which the discretization of the membrane moves with the body [2]. In our study, taken as a reference for validation in particular as a benchmark, the analysis of a deformable solid is treated through a discretization attached to the material itself, in order to reconstruct deformation and stress in the bulk [4]. However, it should be clarified that the formulation adopted for the present work will be fully Eulerian. Particular attention must be paid to near-wall regions, where the presence of strong gradients makes the simulation more difficult to handle, while increasing its numerical complexity [11]. Although in our case only one deformable solid is studied, it is reasonable to mention a system featuring multiple solid bodies and the difficulty that arises when one aims to describe close-range interactions and contacts, which can become a practical bottleneck [16]. This is one of the reasons why a fully Eulerian fixed-grid setting becomes attractive thanks to its high scalability compared with the Lagrangian solution; moreover, in this way it is possible to avoid moving meshes and increase robustness over long times.

The fact that fluid and solid are discretized on the same fixed grid allows the elimination of re-meshing even in the presence of large deformations [15]. Another fundamental requirement is the adoption of a one-continuum setting, in which the fluid and the solid share a single velocity field, whose distinction is performed through a phase indicator, so that the solid contribution enters the equations through a hyperelastic stress term, active only in the solid region [15]. This choice is advantageous when, in addition to the solid, the walls delimiting the domain are also deformable, thereby concentrating the dynamics in near-wall regions and avoiding that the fixed grid must update or adapt the mesh as the channel geometry varies, while keeping the numerical computation stable [11].

In fully Eulerian models, correctly capturing the solid–fluid interface is essential, even

though the body considered is a fully solid one. Its dynamics strongly depends on an accurate reconstruction of the fluid–solid boundary, because it is on such boundary that exchanges of velocity and stresses occur. To describe this effectively, the use of a level set is common, as it represents the interface geometrically, handling contour deformations even when they are large [2]. In long simulations it is known that the use of the level set may introduce volumetric drift, related to advection errors or to re-initialization procedures. This is particularly critical, because the accumulation of error strongly depends on increasing time, thus modifying the global dynamics of the solid [14]. To limit such drift, conservation strategies based on volume corrections or coupling with conservative quantities are adopted, in order to consolidate numerical robustness and prevent interface errors [14].

A conservative alternative is given by representing the solid region through a volume fraction (VOF), which promotes conservation of the solid phase and is suitable for long simulations, performing better than "pure" level set approaches [15]. After clearly describing the interface and volume conservation, the next step is to advect a reliable measure of the finite deformation of the bulk so as to obtain the hyperelastic stress, while maintaining the assumptions made previously [7]. To describe finite deformations and internal stresses without resorting to a discretization that follows the material, a reference map is used, which is an Eulerian field that associates to each point occupied by the solid its position in the initial configuration, tracking the kinematics on the grid. By advecting it in time, a complete Eulerian description is obtained, compatible with large displacements and distortions of the body [7]. Usually, in fully Eulerian methods, the interface and deformation are described by distinct fields, where a possible misalignment leads to erroneous estimates; for this reason, correction procedures for the transport of the deformation variable are introduced [14]. Pressure acts as a Lagrange multiplier associated with the enforcement of the divergence-free constraint; for this reason, such a constraint must be satisfied throughout the considered domain, so as to avoid the appearance of inconsistent pressure fields and spurious forces at the interface, achieved through the extension of the reference map technique to the incompressible case [12]. The literature has also shown that, for long simulations, a conservative and non-dissipative implementation is the best solution to avoid non-physical drifts and preserve the dynamics of the solid, with discrete consistency between transport of the deformation variable and stress computation being decisive [6]. A fundamental practical aspect is the extrapolation of the reference map in the narrow band near the interface, which improves the stability of stress computation and reduces localized errors in the vicinity of the solid–fluid boundary [6]. Recalling that, during deformation transients, the elastic dynamics of the solid can impose a severe constraint on the time step, because the propagation of internal waves must be resolved to avoid instabilities [4]. This constraint is particularly suitable for long simulations, impacting the total cost and making parametrization easier [6]. Such a fully Eulerian description turns out to be the most suitable for the work carried out because, in confined Couette flows, where the shear is persistent with a complex near-wall dynamics, adopting other procedures would lead to erroneous estimates and inconsistent results [10]. In the perspective of long simulations, in order to keep computational costs affordable, it is necessary to use the most efficient possible Poisson solver for pressure (or Helmholtz problems). A possible solution is a finite-difference solver for incompressible flows in which such a problem

is solved through eigenfunction expansions that enable FFT-based implementations [1]; therefore, the fully Eulerian choice is not only modeling-related, but above all it enables the use of faster solvers [1].

A fundamental feature that allows these models to be used for more complex future applications is scalability: indeed, on very large massively-parallel architectures, the efficiency of the solver depends on how communications are organized and, for this purpose, a pencil-distributed solver is proposed, enabling computations on extremely large high-resolution grids, which is very useful in the vicinity of the walls [3]; in particular, it is of fundamental importance for the problem analyzed in the regions where stresses and pressure concentrate, namely near the walls. Concluding, these considerations motivate the choice of a fully Eulerian fixed-grid formulation, aimed at ensuring near-wall robustness and long-time stability in confined flow, as in the present work, namely a pressure-driven constricted channel or a Couette flow adopted for validation.

1.3 Objectives of the work and research questions

In the following paragraphs, the workflow leading from the identification of the fluid–solid two-phase problem to the formulated physical assumptions and the constitutive laws adopted for the solid particle and the elastic walls will be outlined, together with the interface constraints imposed to preserve the continuity of fluid-dynamical and mechanical quantities. Next, the fully Eulerian numerical strategy on a fixed coordinate system will be described, with particular attention to the aspects that make the long-time simulation well-posed and robust—namely mass and volume conservation, interface handling, and consistency between the geometric description and the reconstruction of deformations. To substantiate these statements and assumptions, verification cases based on configurations established in the literature will then be presented, enabling comparisons of velocity and pressure fields, stress distributions and deformation indices, and allowing the definition of accuracy and repeatability criteria. On these bases, the primary investigation will be presented for stiff, walled channels containing a deformable particle, and structured as a parametric study varying the degree of confinement and the relative deformability of the capsule and the wall. The results will be examined to identify how dual compliance affects the transport of the particle through the constricted region, its deformation under maximum confinement, and its downstream recovery after the interaction with the constriction. These aspects are quantified through the evolution of the centroid position, the streamwise centroid velocity, the perimeter variation, and the major-to-minor axis ratio.

Nomenclature

Physical and geometric quantities

Some quantities reported in the following tables are introduced for generality and are used only in specific parts of the manuscript, such as the Couette-flow validation cases discussed in Chapter 4.

Symbol	Meaning
x, z	Streamwise and wall-normal Cartesian coordinates, respectively.
L_x	Streamwise length of the computational domain.
L_z	Wall-normal extent of the computational domain.
H	Nominal channel gap in the reference configuration, used as a characteristic length scale.
a	Initial radius of the deformable solid body.
(c_x, c_z)	Initial coordinates of the body center.
t	Time.
U	Reference velocity scale; in the Couette validation cases, it coincides with the wall velocity used to generate the shear flow.
$\mathbf{u}$	Velocity field.
p	Pressure field.
$\mathbf{f}$	Body-force term appearing in the fluid momentum equation and driving the pressure-driven flow.
f_x	Streamwise component of the body-force density, taken constant and equivalent to an imposed pressure gradient.
$\dot{\gamma}_{ref}$	Reference shear rate used to characterize the pressure-driven confined flow.
$\dot{\gamma}$	Characteristic shear rate; in the Couette validation cases, $\dot{\gamma} = 2U/H$.
ρ_f	Fluid density.
μ_f	Fluid dynamic viscosity.
ν	Fluid kinematic viscosity, defined as $\nu = \mu_f/\rho_f$.
ρ_s	Solid density.
μ_s	Solid viscous contribution, if included in the formulation.
G	Shear modulus of the deformable solid body.
χ	Elastic constitutive coefficient used in the Eulerian hyperelastic formulation; in the present notation, $G = 2\chi$.
$\mathbf{B}$	Left Cauchy–Green deformation tensor.
$\boldsymbol{\sigma}_b$	Hyperelastic Cauchy stress in the solid bulk.
G_w	Shear modulus, or equivalent elastic modulus, of the deformable wall.
h_w	Wall thickness.
$\boldsymbol{\sigma}_w$	Wall stress tensor.

Table 1.1: Physical and geometric nomenclature used throughout the manuscript.

Symbol	Meaning
ϕ_b	Level-set function associated with the deformable solid region and used to identify its interface with the surrounding fluid; in the present implementation, it can also be used to describe the deformable walls.
H_ε	Regularized Heaviside function used to smooth the interface.
ε	Numerical thickness of the regularized interface.
$\mathbf{Y}(\mathbf{x}, t)$	Reference map, or backward characteristics map.
$\mathbf{F}_b$	Eulerian forcing term associated with the elastic response of the solid body.
Re	Reynolds number, measuring the ratio of inertial to viscous effects.
Ca	Capillary number, measuring the ratio of viscous to elastic effects in the deformable body; in the present formulation, $Ca = \mu_f \dot{\gamma}_{ref} a/G = \mu_f \dot{\gamma}_{ref} a/(2\chi)$.
λ	Viscosity ratio, defined as $\lambda = \mu_s/\mu_f$, if applicable.
ρ_s/ρ_f	Density ratio between solid and fluid.
Δt	Time step.
$\Delta x, \Delta z$	Grid spacing in the streamwise and wall-normal directions.
$\mathcal{A}$	Discrete advection operator.
$\mathcal{L}$	Discrete Laplacian operator.
$\mathcal{G}$	Discrete gradient operator.
$\mathcal{D}$	Discrete divergence operator.
Φ	Pressure-correction variable used in the projection step.

Table 1.2: Numerical quantities and dimensionless numbers used throughout the manuscript.

Chapter 2

Physical model and governing equations

2.1 Physical model and assumptions

In this chapter, the physical model under consideration and the main assumptions adopted are described, in order to analyze the fluid–structure interaction mechanisms that develop between the solid particle and the surrounding deformable walls. The system under investigation is introduced below, with its geometry, flow configuration, and modeling assumptions specified so as to obtain consistent numerical results.

The upper and lower boundaries of the channel are no-slip walls, mostly rigid, with two localized deformable portions that are part of the walls themselves. As shown in Fig.1, these deformable wall segments form two inward semicircular constrictions of radius 1, one on the top wall and one on the bottom wall. Embedded in otherwise rigid walls, these soft sections create a localized reduction of the channel width [9]. This modeling choice is intended to make wall deformation more clearly visible and easier to characterize. In the simulations presented below, this constricted region is centered at $x = 4$.

The configuration under investigation is defined within a rectangular computational domain of size $L_x \times L_z$, representing the channel considered in this study, in which the fluid and the deformable solid particle occupy the central region, while the upper and lower boundaries correspond to the deformable walls considered in this work.

A two-dimensional Cartesian reference frame is adopted, with the x-axis aligned with the main flow direction and the z-axis normal to the walls. In particular, periodic boundary conditions are imposed at $x = 0$ and $x = L_x$, so as to represent an ideally infinite channel in the flow direction. Accordingly, the constricted region is identified as the location along x at which, in the reference configuration, the nominal distance between the two walls reaches its minimum value.

The domain contains an incompressible Newtonian fluid. The fluid motion is driven by a constant body-force term acting in the streamwise direction, which is equivalent to an imposed pressure gradient. The deformable walls remain stationary and act as compliant confining boundaries. Starting from a zero-velocity initial condition, the flow develops into a pressure-driven channel flow; in the absence of the immersed particle, the corresponding reference profile is parabolic in the wall-normal direction. The deformable walls do not impose the motion, but respond elastically to the stresses generated by the fluid field and by the interaction with the immersed particle.

In this way, the walls do not act as a kinematic source of the flow, but rather as deformable confining elements that actively participate in the fluid-structure coupling [10, 11]. This is consistent with the overall framework of the present work, in which the focus is on the interaction between a deformable body and deformable walls in a confined channel, as well as with the interpretation of the results in terms of the body response during its passage through the constricted region.

At the fluid–wall interface, the no-slip condition is assumed, so that the local wall and fluid velocities coincide, thereby ensuring kinematic continuity at the interface. The wall motion is therefore determined by the fluid-structure interaction and is evaluated with respect to the initial reference configuration, which includes the constricted profile described above.

A circular solid body, initially undeformed, is placed within the domain, and its deformability is described by a Neo-Hookean constitutive law [4, 2]. Its initial position is identified by the centroid coordinates, x_c and z_c, in the reference configuration. The body is then advected and deformed by the flow as it passes through the confined region. Throughout the thesis, the deformable solid inclusion will be referred to as particle, the streamwise direction will be denoted by x, and the wall-normal direction by z.

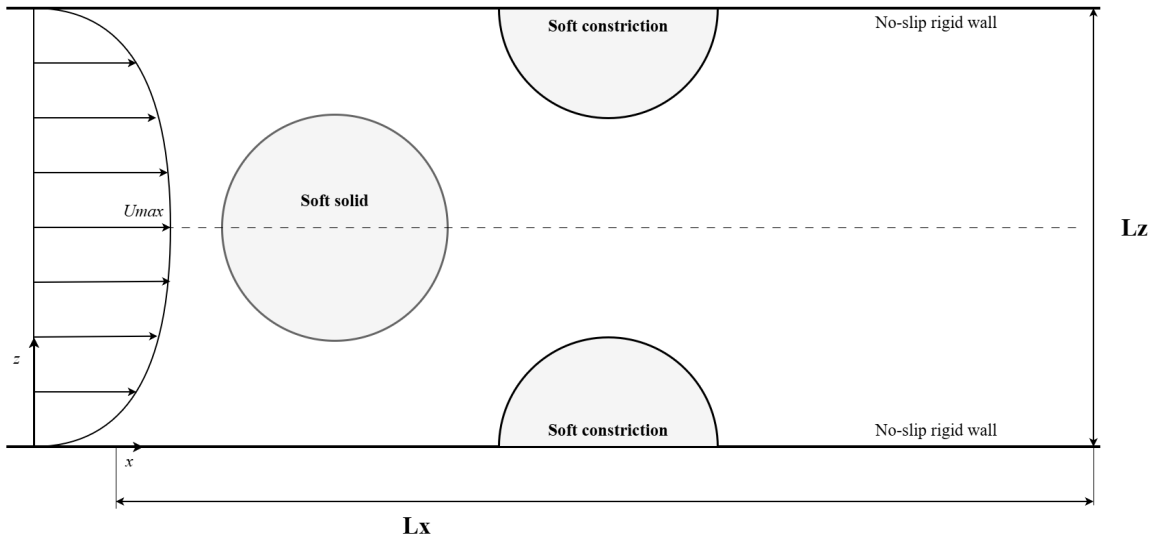

FIG. 1 Schematic of the computational domain for the pressure-driven channel-flow configuration with a deformable solid particle and compliant walls.

2.2 Fluid equations

In this context, the assumption of an incompressible Newtonian fluid within the considered domain is fundamental, because it excludes local volume variations during motion. In other words, a fluid element cannot expand or contract and, at the same time, the solid element can only change its shape without volume variations. The velocity field is defined as $\mathbf{u}(X, Z, t)$ in two dimensions and is composed of the components along X and Z, dependent on time.

The governing equations are expressed by enforcing mass conservation and momentum balance, written in local form. In the present configuration, the fluid motion is driven by a body-force term acting in the streamwise direction, while the fluid–structure interaction contributions

associated with the deformable solid will be detailed later in the Numerical Methods chapter.

From a mathematical standpoint, mass conservation is expressed as:

$$\frac{\partial \rho}{\partial t} + \nabla \cdot (\rho \, \mathbf{u}) = 0. \tag{2.1}$$

For a constant density, this leads directly to the condition:

$$\nabla \cdot \mathbf{u} = 0 \tag{2.2}$$

which imposes a divergence-free velocity field, thus ensuring deformations that change shape without altering the local volume of the domain and that the resulting dynamics are consistent with the physics of the flow and with the response of deformable walls. This aspect is crucial in wall regions exhibiting high compliance, where pressures and shear stresses take on considerable values. This entails the risk that small violations of the incompressibility condition may lead to incorrect estimates of deformations.

The Navier–Stokes equation is obtained by formulating the local momentum balance over a control volume. The temporal accumulation term of momentum is balanced by the convective transport of momentum through the control surface, by surface forces attributable to pressure contributions and viscous stresses, and by body forces acting throughout the fluid domain. For a Newtonian fluid, the differential form of the balance reads:

$$\rho \left(\frac{\partial \mathbf{u}}{\partial t} + (\mathbf{u} \cdot \nabla)\mathbf{u} \right) = -\nabla p + \nabla \cdot \left[\mu \left(\nabla \mathbf{u} + (\nabla \mathbf{u})^T \right) \right] + \mathbf{f}. \tag{2.3}$$

where ρ is the density, $\mathbf{u}$ the velocity field, p the pressure, μ the dynamic viscosity, and $\mathbf{f}$ a body force driving the flow. In the present configuration, this term represents a constant volumetric forcing acting in the streamwise direction, equivalent to an imposed pressure gradient. In the incompressible case, the momentum equation is therefore complemented by the divergence-free constraint introduced above. This condition prevents small numerical violations of incompressibility from altering the estimate of pressure and shear and, consequently, the predicted deformation of the solid; it becomes even more important in the present study due to the presence of compliant walls.

2.3 Non-dimensionalization

To enable comparisons among systems characterized by different geometric and kinematic scales, in order to have a coherent representation of the system kinematics, reference quantities are introduced: characteristic velocity U, characteristic length L and a viscosity scale μ_0 (in the present work typically taken equal to the fluid viscosity, $\mu_0 = \mu_f$). By non-dimensionalizing the variables, the governing equations can be rewritten in the following dimensionless form:

$$\frac{\partial \mathbf{u}}{\partial t} + (\mathbf{u} \cdot \nabla)\mathbf{u} = -\nabla p + \frac{1}{Re} \nabla \cdot \left[\mu \left(\nabla \mathbf{u} + (\nabla \mathbf{u})^T \right) \right] + \mathbf{f}, \tag{2.4}$$

where the Reynolds number appears, defined as:

$$Re = \frac{\rho U L}{\mu_0}. \tag{2.5}$$

which represents the ratio between inertial and viscous forces. In our study it will tend to have a low value ($Re < 1$), consequently viscosity will be much more influential than inertia in determining pressure fields and shear stresses.

To properly describe this work, the Reynolds number alone is not sufficient, therefore we make use of other dimensionless numbers. A first fundamental parameter is the capillary number, which measures the ratio between the viscous forces imposed by the flow and the elastic forces that oppose the deformation of the body.

In the present configuration, the characteristic viscous forcing is associated with the pressure-driven channel flow developing in the confined domain. Since the fluid motion is generated by a constant body-force term acting in the streamwise direction, rather than by wall motion, a reference shear rate $\dot{\gamma}_{ref}$ is introduced to characterize the intensity of the flow-induced stresses acting on the deformable body. Accordingly, the capillary number is defined as:

$$Ca = \frac{\mu_f \dot{\gamma}_{ref} a}{G}, \tag{2.6}$$

where a is the characteristic length of the body, which in our case is the initial radius, and G is the shear elastic modulus of the body material. The capillary number therefore expresses the ratio between the viscous stresses associated with the reference channel flow and the elastic response of the deformable body.

For the Couette-flow validation cases discussed in Chapter 4, the capillary number can be written in explicit form by introducing the characteristic shear rate associated with wall-driven shear flow. In this case, the characteristic shear rate is:

$$\dot{\gamma} = \frac{2U}{H}. \tag{2.7}$$

Therefore, the capillary number is defined as:

$$Ca = \frac{\mu_f \dot{\gamma} a}{G}, \tag{2.8}$$

where a is the characteristic length of the body, which in our case is the initial radius. G is the shear elastic modulus of the body material. Substituting the expression for the Couette shear rate gives[4]:

$$Ca = \frac{2\mu_f U a}{HG}. \tag{2.9}$$

The deformability of the solid body is represented by the shear modulus G, which quantifies the elastic resistance of the material to deformation. Since it appears in the denominator, it follows that the capillary number directly expresses the ratio between the viscous stresses imposed by the flow and the elastic response of the solid. In particular, small values of Ca

correspond to relatively rigid particles. In this context, a Ca smaller than 1 is adopted. In the hyperelastic formulation adopted in the next section, the same elastic resistance is represented through the constitutive coefficient χ. In the present notation, the relation between the two parameters is $G = 2\chi$, therefore the capillary number can equivalently be written as:

$$Ca = \frac{\mu_f \dot{\gamma}_{ref} a}{2\chi}. \tag{2.10}$$

2.4 Hyperelastic capsule model (bulk)

The model adopted to represent the particle hyperelasticity is formulated based on the work proposed by Desmonds et al.[2]. The idea behind their work is that the elastic response of the material does not depend on a linear relation between stresses and strains, but derives from an energy function ϵ_b , which is linked to the deformation through the deformation gradient $\nabla_e X$. In the studied case the material is assumed isotropic and the energy independent of the reference frame, so that the left Cauchy-Green tensor (B) can be used for the description.

Since the adopted formulation is fully Eulerian, instead of directly using the Lagrangian map X, the backward characteristics map Y(x,t) is used, called so because it connects the current position on the Eulerian grid to the previous configuration[7, 12]. Following this procedure, the tensor B is related to $\nabla_e Y$ through the relation:

$$\mathbf{B}(\mathbf{x}, t) = \left[\nabla_{\mathbf{x}} \mathbf{Y}\right]^{-1} \left[\nabla_{\mathbf{x}} \mathbf{Y}\right]^{-T}. \tag{2.11}$$

Considering a Neo-Hookean law to identify the elastic response of the bulk, in which the energy depends only on the trace of the tensor Tr(B). It follows that the Cauchy stress in the bulk is proportional to B, with χ representing the elastic constitutive coefficient:

$$\sigma_b = 2\chi\, \mathbf{B}. \tag{2.12}$$

In the present formulation, the constitutive coefficient χ is directly related to the shear modulus G used in the definition of the capillary number in Section 2.3. By comparison with the standard Neo-Hookean form, one obtains:

$$G = 2\chi. \tag{2.13}$$

Therefore, the parameter G used in the dimensionless analysis and the coefficient χ appearing in the constitutive law describe the same elastic resistance of the solid body. The mechanical response is determined by the deformation gradient and by the Cauchy tensor.

2.5 Quantities of interest and metrics

To describe the behavior of the system, the analysis of the results is based on a set of quantities of interest capable of representing both the motion dynamics and the deformation of the solid. In particular, attention is focused on the position of the centroid, its evolution over time, and the velocity of the centroid in the main flow direction, which constitutes the most relevant kinematic

quantity for interpreting the transport of the body inside the channel[9].

Alongside the kinematic quantities, the evolution of the shape of the solid during its passage through the constriction and the downstream region is also considered. To this end, in addition to the qualitative observation of the profiles, two particularly useful geometric quantities are introduced: the perimeter of the solid and the ratio between the major and minor axes. These quantities are evaluated for a representative configuration, chosen when the body is located at the center of the constriction, that is, in the region where confinement effects are most intense[9].

The perimeter provides an overall measure of the stretching and deformation of the contour, while the ratio between the major and minor axes makes it possible to quantify directly the degree of shape anisotropy. In this way, it is possible to compare the different simulated cases more clearly, relating the dynamics of the centroid to the geometric response of the solid and to the different role played by the relative deformability between the particle and the walls.

Chapter 3

Numerical methods and implementation

The numerical framework employed in this work is based on a computational code originally developed at KTH for the simulation of deformable capsules in viscous flows. The code itself was not developed as part of this thesis. The present work focused on adapting and extending the existing solver to address the specific fluid-structure interaction problem considered here. In particular, the original formulation for deformable capsules was modified in order to treat elastic solid bodies, and the smoothed Heaviside function used in the Eulerian representation was revised accordingly. In addition, the treatment of the confining walls was adapted to reproduce the partially circular constraints of the present geometry. The numerical methods described in this chapter are therefore based on the original KTH solver, with the above modifications introduced during the thesis work to make it suitable for the present application.

3.1 Numerical discretization and solution of the fluid problem

Although the case is physically two-dimensional, in this work the simulations are performed using a three-dimensional solver. The 2D configuration is obtained by enforcing the absence of variations in the third direction by imposing invariance of the dynamics along that axis[1]. To solve the incompressible Navier-Stokes equations describing the present case, an incremental pressure-correction scheme is adopted, in which incompressibility is enforced by solving a Poisson problem for a pressure correction. Time advancement is performed using an explicit method, namely a third-order low-storage Runge–Kutta scheme. To describe this system, it is convenient to introduce the kinematic viscosity defined as $v = \mu/\rho$ and to consider pressure scaled by density. The discretization of the equations is carried out on a structured Cartesian grid with staggered (MAC) arrangement, i.e., the different variables (velocity and pressure) are not all located at the same point but are staggered. In particular, pressure is located at the cell center while velocity is imposed at the walls. This improves the pressure-velocity coupling and the quality of the incompressible projection. Since periodic boundary conditions are prescribed along the X direction, the grid spacing is uniform along that direction, whereas along Z a non-uniform grid is adopted to resolve strong spatial gradients in the vicinity of the walls, these gradients are approximated using second-order finite differences.

Notation in terms of discrete operators

To describe the time-advancement scheme in a compact way, the discrete operators appearing in the semi-discrete formulation of the equations are introduced and defined as:

- $\mathcal{A}(\mathbf{u})$ denotes the discrete operator associated with the convective (advection) terms in the momentum equation, evaluated from the velocity field $\mathbf{u}$;
- $\mathcal{L}$ denotes the discrete Laplacian operator, used to represent the viscous diffusive term;
- $\mathcal{G}$ denotes the discrete gradient operator (applied to pressure or to the pressure correction);
- $\mathcal{D}$ denotes the discrete divergence operator (applied to the velocity field).

In order to ensure an effective projection onto the incompressibility constraint, the operators are chosen in a consistent way, typically such that the Laplacian is compatible with the divergence–gradient composition (i.e., $\mathcal{L} \approx \mathcal{D}\mathcal{G}$ in the adopted discretization). With this notation, the prediction–correction sequence enforcing $\nabla \cdot \mathbf{u} = 0$ can be written in semi-discrete form and applied at each sub-step of the Runge–Kutta scheme (index k), clearly highlighting the role of the operators $\mathcal{A}$, $\mathcal{L}$, $\mathcal{G}$ and $\mathcal{D}$ in the development of the algorithm. At each Runge–Kutta step, a predicted velocity is computed by integrating the momentum equation; it must be specified that the field $\mathbf{u}^*$ is not solenoidal, i.e., it does not satisfy the divergence-free condition.

$$\mathbf{u}^* = \mathbf{u}^k + \Delta t \left(\alpha_k (\mathcal{A}\mathbf{u}^k + \nu \mathcal{L}\mathbf{u}^k) + \beta_k (\mathcal{A}\mathbf{u}^{k-1} + \nu \mathcal{L}\mathbf{u}^{k-1}) - \gamma_k \mathcal{G} p^{k-1/2} \right). \tag{3.1}$$

The incompressibility condition is then enforced by solving a Poisson equation for the pressure correction, formulated by requiring the corrected velocity to be divergence-free, as follows:

$$\mathcal{L}\Phi = \frac{\mathcal{D}\mathbf{u}^*}{\gamma_k \Delta t}. \tag{3.2}$$

The velocity is projected onto the space of solenoidal fields by subtracting the gradient of the correction; subsequently, pressure is updated incrementally by adding Φ to the pressure at the previous half-step.

$$\mathbf{u}^{k+1} = \mathbf{u}^* - \gamma_k \Delta t \, \mathcal{G}\Phi, \qquad p^{k+1/2} = p^{k-1/2} + \Phi. \tag{3.3}$$

As mentioned above, time integration relies on a third-order low-storage Runge–Kutta scheme, where the coefficients provide the combination of contributions to be evaluated at the subsequent sub-steps, given by:

$$\alpha = \{8/15,\ 5/12,\ 3/4\}, \qquad \beta = \{0,\ -17/60,\ -5/12\}, \qquad \gamma = \alpha + \beta. \tag{3.4}$$

In the present study, since the regime involves a low Reynolds number, the viscous restriction on the time step becomes relevant, making an implicit treatment of the diffusive terms possible. A more computationally efficient strategy, applicable when grid refinement is concentrated in Z, consists in making only the diffusion in Z implicit, thus addressing the problem through one-dimensional tridiagonal systems.

$$\mathbf{u}^{**} = \mathbf{u}^k + \Delta t \left(\alpha_k \mathcal{A}\mathbf{u}^k + \beta_k \mathcal{A}\mathbf{u}^{k-1} + \gamma_k \left(-\mathcal{G} p^{k-1/2} + \nu \mathcal{L}\mathbf{u}^k \right) \right). \tag{3.5}$$

The pressure update equation is expressed as follows:

$$p^{k+1/2} = p^{k-1/2} + \Phi - \gamma_k \frac{\nu \Delta t}{2} \mathcal{L}\Phi. \tag{3.6}$$

Whereas the variant with only Z implicit is:

$$\mathbf{u}^* - \gamma_k \frac{\nu \Delta t}{2} \mathcal{L}_z \mathbf{u}^* = \mathbf{u}^{**} - \gamma_k \frac{\nu \Delta t}{2} \mathcal{L}_z \mathbf{u}^k. \tag{3.7}$$

With regard to the forcing term $\mathbf{F}_b$, associated with the fluid–structure interaction, it is included in the velocity-prediction step and integrated in time consistently with the RK scheme:

$$\mathbf{u}^* = \cdots + \Delta t \left(\alpha_k \mathbf{F}_b^k + \beta_k \mathbf{F}_b^{k-1} \right). \tag{3.8}$$

The entire procedure described above is required to ensure incompressibility enforcement at each time step, thus providing the numerical basis for the coupling among deformable solids.

3.2 Eulerian interface and fluid–structure coupling

In order to numerically distinguish between fluid region and solid region, a level set function ϕ_b is introduced, i.e., a signed scalar function that implicitly represents the interface between the two phases[14, 2]. The motion follows the advection law:

$$\partial_t \phi_b + \mathbf{u} \cdot \nabla \phi_b = 0. \tag{3.9}$$

The transport of the level set is performed using the same velocity field employed to analyze the evolution of the coupled system. The update is carried out through a high-resolution advection scheme, so that the numerical diffusion of the interface is limited, preserving its localization[14]. The quality of the interfacial reconstruction directly affects the distribution of the elastic term in the momentum equation.

The fluid–structure coupling is represented in the Eulerian equations through the addition of a force term associated with the elastic stresses of the Neo-Hookean solid, which depends on the divergence of the Cauchy stress and is weighted by a Heaviside function:

$$\mathbf{F}_b = \nabla \cdot \left(H\left(\frac{\phi_b}{\varepsilon} \right) \boldsymbol{\sigma}_b \right), \qquad \boldsymbol{\sigma}_b = 2\chi\, \mathbf{B}. \tag{3.10}$$

Alongside the level set function, the reference map is introduced, which makes it possible to reconstruct the internal state of deformation of the solid region. A grid that follows the material is not required, because each point in the current configuration is associated with the corresponding position in the initial configuration. The reference map is updated in a fully Eulerian form, through a transport equation consistent with that used for the interface. In this way, the shape and the deformation state evolve consistently within the same numerical formulation.

The elastic contribution is introduced into the equations of motion in conservative form,

through the divergence of the stress weighted by a localization function. This turns out to be the best choice when considering long-duration simulations, because it makes it possible to avoid the appearance of spurious forces while maintaining a better reconstruction of the numerical problem.

In particular, in this work the same Heaviside function proposed by Desmond et al.[2] is not used; instead, a "smoothed" function is chosen so that the transition between the solid and liquid phases is not sharp, but rather gradual, in order to obtain a more accurate representation in the neighborhood of the particle boundary. This equation was proposed by Popinet in 2018 [8] and is defined as follows:

$$H_\varepsilon\big(\phi(\mathbf{x})\big) = \begin{cases} 0, & \text{if } \phi(\mathbf{x}) < -\varepsilon, \\ 1, & \text{if } \phi(\mathbf{x}) > \varepsilon, \\ \dfrac{1 + \phi/\varepsilon + \sin\big(\pi\phi/\varepsilon\big)/\pi}{2}, & \text{otherwise.} \end{cases} \tag{3.11}$$

3.3 Numerical handling of deformable walls

The walls are treated as additional deformable bodies embedded in the same fully Eulerian formulation adopted for the particle. Their mechanical state is therefore reconstructed on the fixed grid through a reference-map-based description, consistently with the strategy used for the immersed solid. This allows the wall deformation to be coupled to the fluid motion without introducing a separate moving mesh or an independent Lagrangian discretization[16]. For the main physical configuration investigated in this thesis, the walls do not prescribe the fluid motion. The flow is pressure-driven through a constant body-force term acting in the streamwise direction, while the walls remain stationary in the reference configuration and deform only in response to the stresses transmitted by the fluid and by the interaction with the particle. Their numerical role is therefore that of compliant confining boundaries, whose deformation modifies the local fluid–structure coupling without acting as a direct kinematic forcing mechanism. The same numerical formulation can also be employed in validation cases based on wall-driven shear flows. In those benchmark configurations, such as the Couette flow tests discussed in Chapter 4, the wall velocity is prescribed in order to reproduce the reference setup available in the literature[15].

3.4 Simulation settings and post-processing

The simulations presented below were carried out using a structured Cartesian grid, varying the resolution in order to adequately represent both the deformable body and the walls, where the highest stresses are concentrated and the pressure and velocity gradients are high[11].

It should be specified that the case is two-dimensional, while the solver used is three-dimensional. This does not affect the analysis of the system, since invariance is imposed along the third direction (in our case, the y-direction). The resolution actually employed in the cases analyzed was selected on the basis of the tests performed in the following validation chapter,

choosing it according to the quality of the results obtained and the convenience in terms of computational costs.

The time step is determined by imposing stability criteria consistent with the FSI problem under study, taking into account the elastic response of the body and the walls, and not only the convective and viscous restrictions of the fluid-dynamic problem. The adopted value is selected so as to ensure a stable and sufficiently accurate temporal evolution of all the fields involved[4].

The isolated cases are organized as a parametric study, in which the stiffness is varied for both the immersed solid and the walls, while keeping the remaining working parameters that define the problem constant. The controlled variation of these parameters makes it possible to carry out an accurate analysis of the double compliance present. For each simulation, the main fields of interest are saved at regular intervals, so as to reconstruct the global and local evolution of the system. The time instants shown in this work are the most significant ones, representing the physical events that occur during the development of the problem.

Post-processing is carried out by analyzing specific quantities of interest explained in detail in the following chapters, which relate the behavior of the solid and the walls to the dynamics of the system and to its own evolution. The main quantities of interest will be the position of the body and the trajectory of its centroid.

Finally, to make the comparison among the different cases clearer, the results were organized according to a uniform structure, reporting for each simulation the parameters used and the quantities extracted to perform the analysis. This makes it possible to interpret in an orderly way how these parameters influence the dynamics of the system, so that a coherent study of the entire formulation of the problem is obtained.

Chapter 4

Validation

This chapter addresses the verification and validation of the adopted numerical model; this serves to demonstrate the reliability of the subsequent work, both in terms of the physical system and from a computational standpoint. This step is of fundamental importance in the present study, since the configuration considered consists of a confined fluid-structure interaction problem, in which the deformation of the solid and the consequent modification of the interface are non-negligibly influenced by the choices of spatial and temporal discretization, as well as by the selection of the numerical parameters employed for this purpose. The process is carried out by reproducing a validation case inspired by the literature; in particular, it considers the configuration developed by Gao et al. [4] and later revisited by Sugiyama et al.[15], which features two deformable particles in a confined Couette flow, selected to ensure a proper resolution of the close-interaction phases, during which the dynamics become numerically more challenging. The examined morphology thus plays a fundamental role, as it introduces a fluid–structure coupling that depends on the adopted numerical discretization, thereby incorporating the essential elements of a fluid–structure interaction and elucidating viscous dynamics together with the response of the embedded solids. The motivation for considering several existing benchmark replications lies in the integration of the essential content that can be obtained from each problem, thereby enabling a validation of what is presented subsequently, in a manner consistent with everything that has been explained and developed in the present work. The reliability of the validation is assessed through the evaluation of several criteria, not only in terms of instantaneous configurations, but also in terms of morphological evolution, the evolution of trajectories at characteristic times, and the final equilibrium configuration. These considerations are evaluated so as to obtain, as a final outcome, a sufficiently robust numerical setup, such that the behavior of the system components can be regarded as a physical effect rather than an artifact due to discretization.

4.1 Literature benchmark: two particles in confined shear

The considered domain consists of a two-dimensional rectangular box developed along the x and z axes, where x is the flow direction while z is the wall-normal direction, with dimensions $L_x \cdot L_z = (8 \cdot 4)$. Inside the incompressible Newtonian fluid, two identical solids A and B are present, hyperelastic and deformable, coupled through a fluid-solid interface enforcing velocity continuity and traction balance, with radius $r = 0.5$, centered at the coordinates $x_{c,A} = (2, 2.5)$

and $x_{c,B} = (6, 1.5)$, respectively, as shown in the figure below. The system is configured as a Couette flow: at the initial instant the pressure field is uniform and the velocity field is zero, while the motion develops following the start-up (at $t = 0$) of the movement of the lower and upper walls, assumed rigid. The walls, on which the no-slip condition is imposed, are located at $z = 0$ and $z = 4$ and move in the x direction with opposite directions, with velocities $V_{\text{upper}} = 1$ and $V_{\text{lower}} = -1$, respectively; the boundary conditions in the streamwise x direction are periodic between $x = 0$ and $x = L_x$ for the velocity and pressure fields. The parameterization of the case, considered in the low Reynolds number regime, is implemented by setting the fundamental variables $Re = 0.1$ and $Ca = 0.25$, in agreement with the work by Gao et al.[4], in which the benchmark itself fixes the deformability, namely an elasticity-controlled deformation under shear regime, such that the magnitude of deformation is determined primarily by the elastic properties of the solid with respect to the imposed shear. The material properties are density $\rho = 1$, fluid and solid phase viscosities (the solid phase being assumed purely elastic) $\mu_f = 20$, $\mu_s = 0$, and shear modulus $G = 40$.

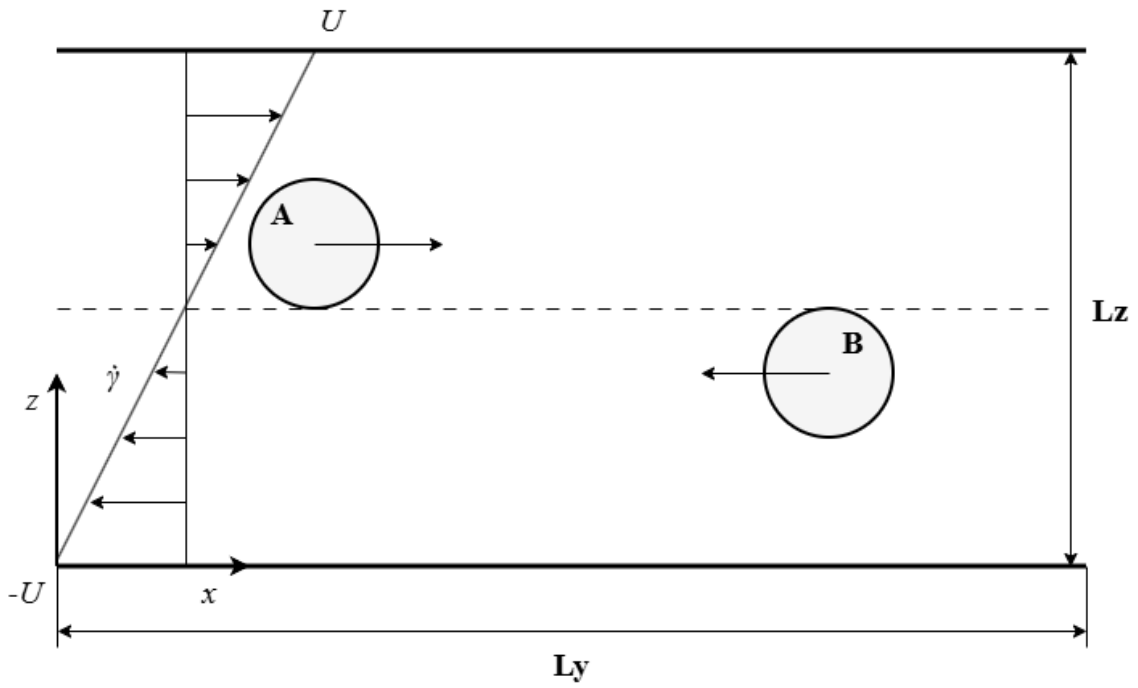

FIG. 2 Schematic of the computational domain for plane Couette flow with counter-moving walls. The upper wall moves with velocity U, while the lower wall moves with velocity $-U$, generating a shear flow of rate $\dot{\gamma}$. Two circular particles, denoted by A and B, are suspended inside a domain of size $L_y \times L_z$.

In this configuration, the aim is to assess the solver's ability to reproduce the different physical phases occurring in the interaction between two deformable particles, which, during the simulations, come into close proximity, leading to a high numerical difficulty. This validation is discussed qualitatively, by considering instantaneous positions and morphology, and quantitatively, by focusing on the evolution of the trajectory.

The interaction phases, shown in Fig. 4, can be described as follows:

- **Initial deformation:** In the first instants, once the shear has developed, the particles deform rapidly, assuming an elliptical shape with an orientation consistent with the shear

direction. This transition is very fast, increasing rapidly in the first instants and then varying gradually throughout the process, thus indicating an initial adaptation to the imposed flow. It is important to determine the configuration with which the particles enter the approach phase, thereby influencing the first encounter.

- **Approach and first encounter:** As time progresses, the particles move within the domain, approaching each other. The reduction of the inter-particle distance leads to an increase in the system dynamics, where interactions are more intense and sensitive. In the vicinity of the approach, more pronounced deformations and orientations can be observed.
- **Roll over:** In the first close encounter, the dynamics can be traced back to the experiment of Gao et al., and the system enters the roll-over mode, in which the relative arrangement of the pair changes because one particle tends to overtake the other while the overall configuration tends to rotate.
- **Bounce back:** After the first interaction events, the dynamics is no longer dominated by the roll-over mode, but can be traced back to a behavior referred to as bounce back. The particles tend to arrange themselves in opposite regions of the channel, and their re-approach leads to a reorganization that reverses the relative motion, producing this rebound.
- **Relaxation and equilibrium:** As the simulation time increases, the strength of the interactions weakens, leading to a smaller variation in positions and to the stability of the particle positions. The final configuration is compatible with what is expected from the benchmark and provides a qualitative basis for the qualitative comparison in the next figure.

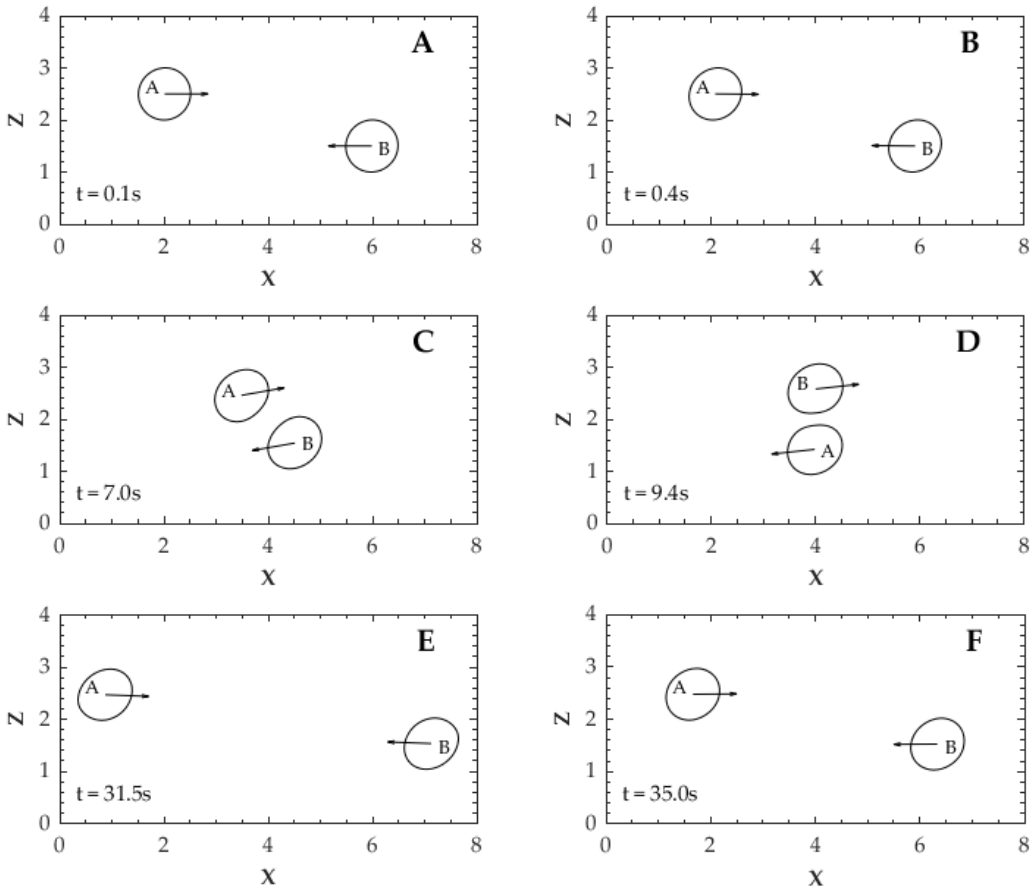

FIG. 3 Temporal evolution of the configuration of the two particles in the X-Z plane.

For a quantitative analysis, the trajectory followed by the centroids of the two particles during the simulation is considered; in particular, the wall-normal coordinate of the respective centroids is plotted as a function of time, as shown in Fig. 2. Peaks and troughs act as markers of the phases described above, enabling a direct comparison with the benchmark. Comparing different grid resolutions is essential to assess the numerical sensitivity, which tends to manifest itself in the phases where the distance between particles is minimal.

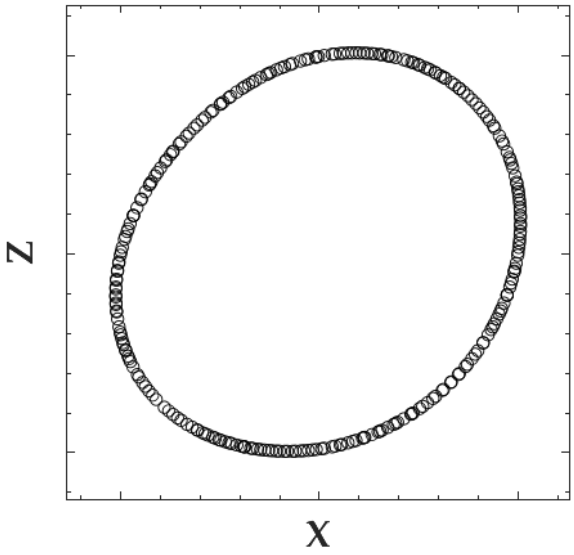

FIG. 4 Equilibrium shape of the particle. Open circles represent the particle interface at $t = 60.0$ s under the considered flow conditions.

In the initial stage, the variation becomes more evident because the particles quickly enter the interaction regime, which represents a preparation phase for the first encounter. This first encounter corresponds to the first maximum; as stated above, this peak is associated with the roll-over event, thus highlighting the usefulness of this plot, which makes it possible to localize in time the events identified qualitatively from the previous snapshots. At the peaks, the distance between the particles is minimal, because more intense hydrodynamic forces are induced, which depend on a "squeezing" effect: the fluid trapped in such a thin gap must escape rapidly, but the rapid increase in viscous resistance tends to generate large forces that oppose this approach. Subsequently, the particles enter the next bounce-back phase, showing an alternating behavior in which they tend to occupy the two opposite half-sections of the domain of interest, thereby leading the particles to reorganize. As the simulation time increases, the amplitude of these variations gradually decreases, indicating that the particles tend to stabilize.

4.2 Convergence study and numerical sensitivity

This section aims to assess the numerical sensitivity of the two-particle benchmark with respect to the spatial discretization, focusing on the solver's ability to reproduce the expected physical behavior of the reference case under consideration. In this context, different grid resolutions produce observable differences among the various profiles, reflecting the different level at which the interface, the deformation, and the gradients arising during the closest interaction phases are resolved. The main objective is to verify that the overall structure of the dynamics is preserved and that the temporal evolution of the particles remains consistent with that described by the reference benchmark.

The comparison is carried out by considering the wall-normal coordinate of the centroid, $z_c(t)$, for both particles as a function of time. In order to better highlight the variations, only $z_c(t)$ is evaluated, since it is more significant than $x_c(t)$. As previously discussed, the motion mainly

develops along the streamwise direction, and therefore the latter does not provide particularly useful information for identifying the characteristic events of the interaction.

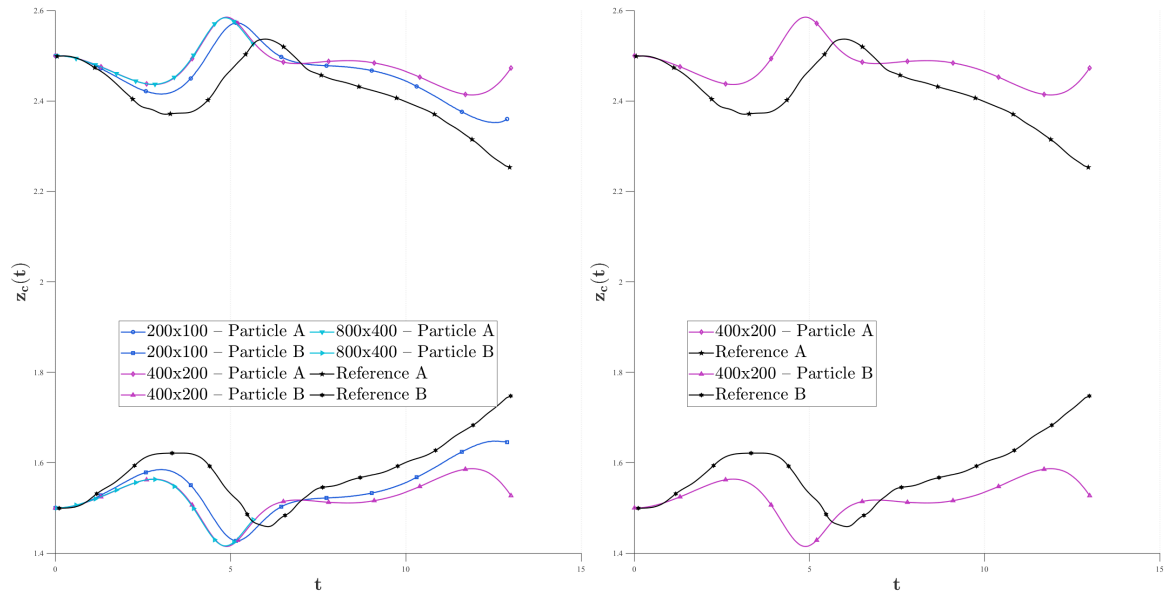

FIG. 5 Comparison of the vertical particle position $z_c(t)$ as a function of time for different grid resolutions against the reference solution.

In all the curves, the same sequence of physical events can be identified. In the initial stage, a rapid variation of $z_c(t)$ appears, which corresponds to the adaptation of the particles to the imposed motion and to their entrance into the interaction regime. This behavior represents the preparation for the first significant approach. Subsequently, the first maximum of the curve appears, which identifies the first close encounter between the two particles. At this stage, the system enters the roll-over mode and the inter-particle distance reaches its minimum.

After this maximum, the trajectory evolves toward a minimum point, which can be interpreted as the consequence of the reorganization of the pair after the first encounter. In this phase, the system is no longer dominated only by roll-over, but enters the bounce-back regime already described in the previous section. This minimum represents a change in the dynamical configuration of the system: indeed, the particles tend to arrange themselves in opposite regions of the channel cross-section, and their relative motion is progressively reversed.

The behavior after these stages is analogous, with alternating maxima and minima of progressively reduced intensity. This damping is due to the fact that the system gradually loses the intensity of the initial interactions and progressively tends toward a more stable configuration. This behavior is consistent with the benchmark, in which the final part of the evolution is characterized by a progressive reduction in the amplitude of the centroid variations.

From a numerical point of view, the differences among the various resolutions mainly emerge precisely at these maxima and minima. These phases are also the most challenging from the solver perspective, because under such minimum-gap conditions the squeezing effect increases, making the resolution of the flow fields and the computation of the stresses more delicate.

For this reason, the coarsest grid tends to return smoother peaks and a slightly less accurate temporal localization of the extrema, whereas the finer grids are able to describe the structure of

the signal more faithfully.

Consequently, the convergence test can be considered satisfactory for the purposes of the present work. Although the discretization adopted for the subsequent simulations is lower than that of the reference case, it is still adequate to reproduce the main physical events of the benchmark and to describe its temporal evolution reliably.

4.3 Checks on deformable walls

In addition to the previous benchmarks, some consistency checks were carried out on the numerical treatment of the deformable walls. The objective of these checks is not to provide an exhaustive validation of the wall model, but to ascertain that its inclusion in the solver does not introduce non-physical behaviors and that the coupling with the fluid remains consistent with the adopted Eulerian formulation.

In particular, it was verified that the response of the walls remains regular and bounded over time, with no evidence of numerical instabilities. It was also checked that varying the stiffness of the walls produces a response consistent with what can reasonably be expected, namely that stiffer walls tend to reproduce a behavior closer to the rigid limit, while more compliant walls participate more significantly in the interaction with the fluid and with the immersed body.

Overall, these checks indicate that the adopted wall model is numerically consistent for the purposes of the present work and can therefore be used in the subsequent parametric study.

Chapter 5

Results and Discussion

5.1 Objectives of the Chapter

The following chapter is fundamental because it gathers the elements needed to understand the results obtained from the analysis developed in this thesis work. The main interest is to understand how the passage of a deformable solid is influenced by confinement between deformable walls, in terms of shape, position, and transport dynamics. The description is no longer simply qualitative; rather, the results are interpreted as the manifestation of a coupled interaction between the domain geometry, the deformability of the body, and the kinematics of its centroid.

The idea underlying this chapter is that, in problems of this type, the shape of the solid is no longer a secondary consequence of the motion; rather, deformation itself constitutes a true physical variable of the problem. Specifically, it modifies the way in which the solid crosses the confined region, the distribution of stresses at the interface with the fluid, and the position of the centroid. An approach consistent with that adopted in the literature on deformable bodies in confined channels is used, in which the shape and velocity of the particle under consideration are discussed in parallel during the different phases of the problem considered [9].

Consistently with what has been stated, the first objective is to describe clearly the evolution of the shape assumed by the solid during the various phases of the problem. In this regard, particular attention is paid to the way in which the solid, initially having a circular configuration, changes its contour while crossing the constriction and continuing downstream of the duct. The study of the solid morphology provides the most immediate trace of its response to the interaction with the walls, since it is a body that must adapt its contour to the available space. This adaptation represents the image of the balance between the stresses imposed by the flow field and the deformability of the solid itself.

The following objectives consist of examining the final stage of the passage and describing the motion of the solid by focusing on the study of the centroid identified in post-processing. As regards the passage, it should be noted that the solid does not immediately return to its initial shape, but retains the deformation undergone during the crossing. For this reason, the final phase must be considered a distinct phase and not simply a continuation of the motion. In the literature as well, the downstream behavior after the constriction is recognized as physically relevant: the deformation is not always symmetric with respect to the center of the constriction, and shape recovery may occur with a delay that depends on the response time of the deformable body [9]. The choice to focus on the centroid, on the other hand, is based on the possibility of synthesizing the overall evolution of the body through a well-defined quantity that is, above all,

easily comparable between successive instants. Attention is placed on the velocity component in the streamwise direction, since it is the direct representation of the influence of the constriction on the advancement of the solid. In the present discussion, however, the quantitative analysis is centered on the streamwise component, since it is the one for which the most consistent comparison among the selected cases is available.

This methodological choice is consistent with studies in the literature, where the description of deformable bodies is expressed through the same choices adopted to evaluate this work [14].

To conclude, the chapter is organized so as to proceed from the more general picture toward more specific results. The analysis initially focuses on the shape of the solid and then proceeds to the study of its trajectory and centroid velocity, ending with a joint interpretation of these results.

5.2 Parametric study and comparison criteria

The parametric study that makes it possible to analyze the considered system is based on nine different simulations, obtained by combining three values of stiffness for the solid (20, 40, 80) and three values of stiffness for the walls (25, 50, 100). The objective is not to discuss these simulations in isolation, but to show how the response of the system changes as the relative stiffness between the solid and the walls varies, while keeping the other system parameters described previously constant, such as the Reynolds number and the capillarity number.

A study of this type makes it possible to distinguish two complementary lines of analysis. On the one hand, there is the effect of the solid stiffness with the wall stiffness fixed; on the other hand, the reverse. This double reading makes it possible at the same time to isolate the specific role of the two parameters, while also allowing cross-comparisons.

To make the description of this problem and of the considered cases clearer, a unique nomenclature is adopted for each case. The adopted convention consists of indicating each simulation with two pairs of letters and numbers, where W and S indicate the stiffness of the wall and of the solid, respectively, while the numbers represent the actual value of this property for the selected region. The nine cases are therefore identified as $W25$-$S20$, $W25$-$S40$, $W25$-$S80$, $W50$-$S20$, $W50$-$S40$, $W50$-$S80$, $W100$-$S20$, $W100$-$S40$ and $W100$-$S80$. This nomenclature is used only to make the presentation easier and to avoid unnecessary repetition.

As already stated previously, the setting of this problem is focused on the velocity component in the streamwise direction. This choice is adopted because the centroid follows a trajectory that is substantially aligned with the main direction of motion, neglecting any considerations about lateral migration, since the latter is not relevant in the present work.

From a representational point of view, not all time instants are considered, but only those of greatest interest, namely: before entering the constriction, at the center, at the exit, and further downstream. In the same way, the centroid velocity is represented as a function of its position.

It should also be specified that the geometric discussion and the velocity discussion do not rely on exactly the same subset of cases. The shape analysis is mainly supported by the cases for which the perimeter and axis ratio at the center of the constriction are available, namely $W25$-$S20$, $W25$-$S40$, $W50$-$S20$, and $W50$-$S40$. The velocity analysis, on the other hand, is

discussed quantitatively through the cases reported in the table of streamwise velocity extrema, namely *W*100-*S*40, *W*25-*S*40, *W*50-*S*20, *W*50-*S*40, and *W*50-*S*80.

To conclude, an overall view of the simulations will be presented, and then the analysis will proceed to how stiffness influences the behavior of the solid in terms of shape and velocity, initially offering a broader overview and then focusing on the most significant instants, which will be analyzed in greater detail.

5.3 Overview of simulations

The simulations, considered as a whole, show a common behavior, which nevertheless develops differently depending on the combination of the stiffness of the solid and the walls. In all cases, the solid crosses the confined region, modifies its shape during the passage, and reaches a downstream configuration that is still influenced by the interaction with the walls. Therefore, this is not a collection of independent cases, but rather different manifestations of the same physical phenomenon.

It is already possible to recognize clearly evident qualitative differences, the first of which is the morphology of the solid during the passage. In some cases, a much more marked shape variation is observed, whereas in others there is a greater preservation of the initial shape. This difference is not limited to the region of maximum confinement alone, but is also reflected in the shape assumed by the solid in the final stage of the motion.

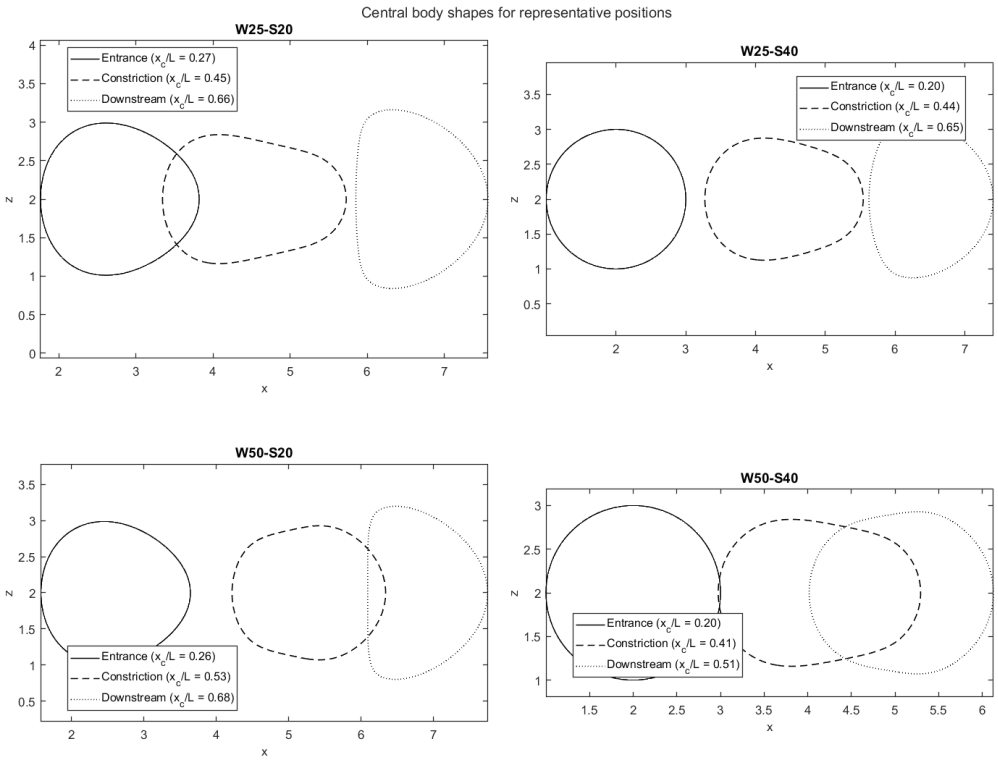

FIG. 6 Representative body shapes for selected cases at three characteristic positions of the motion: entrance, constriction, and downstream region.

This overall comparison provides the qualitative framework for the more focused parametric

analyses discussed below, where shape and transport are examined separately at fixed wall and solid stiffness.

The final stage of the passage differs among the various cases, and it can be noted that in no case does the body completely recover its initial shape. However, in some cases the residual deformation appears more evident, with a final configuration clearly different from the initial one. From a kinematic point of view as well, although the solid remains aligned with the direction of motion throughout the entire phenomenon, it should be emphasized that the variability of the shape affects the velocity of the solid itself. This detail regarding the velocity of the centroid along the main direction of motion confirms that the transport of the body does not evolve identically in all cases. The additional velocity comparisons further show that the overall profile structure is common to all the selected cases, while the amplitude of the extrema and the persistence of the downstream modulation depend on the relative stiffness of the solid and the walls.

5.4 Effect of the solid stiffness at fixed wall stiffness

In this section, the effect of the stiffness of the solid is analyzed while keeping the stiffness of the walls constant. The study focuses on how the stiffness of the body influences its ability to adapt to the constriction, both at the narrowest point and subsequently downstream, with particular attention paid to the shape in these phases. In general terms, it is reasonable to expect that a softer solid, that is, one with lower stiffness, will deform more. This hypothesis is not an absolute rule, but rather a working hypothesis to be compared with the actual results in the different cases.

The first set of cases includes those in which the wall stiffness is equal to 25, making the contribution of the external confinement the least rigid among the considered cases. The comparison is therefore carried out among the softest case with $S = 20$, the intermediate case with $S = 40$, and the stiffest case with $S = 80$. A representative comparison at fixed wall stiffness $W = 25$ is shown in Fig. 7, while the corresponding velocity-only comparison is reported in Fig. 8.

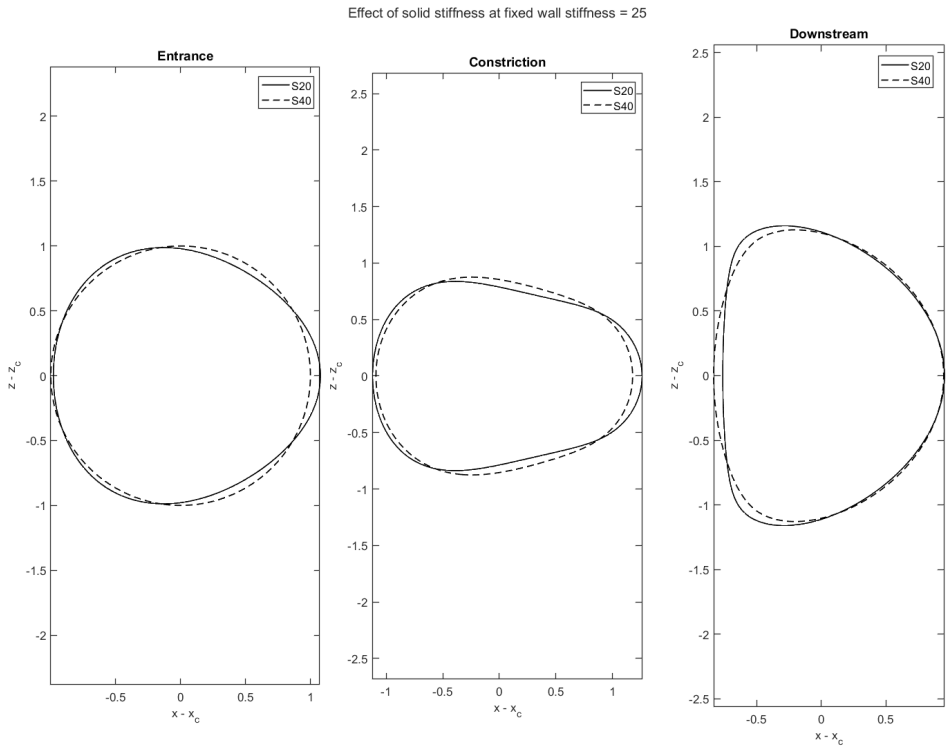

FIG. 7 Effect of the solid stiffness at fixed wall stiffness $W = 25$.

The morphological differences highlighted above are accompanied by corresponding differences in the streamwise transport of the centroid, which make the effect of solid stiffness more evident from a kinematic point of view.

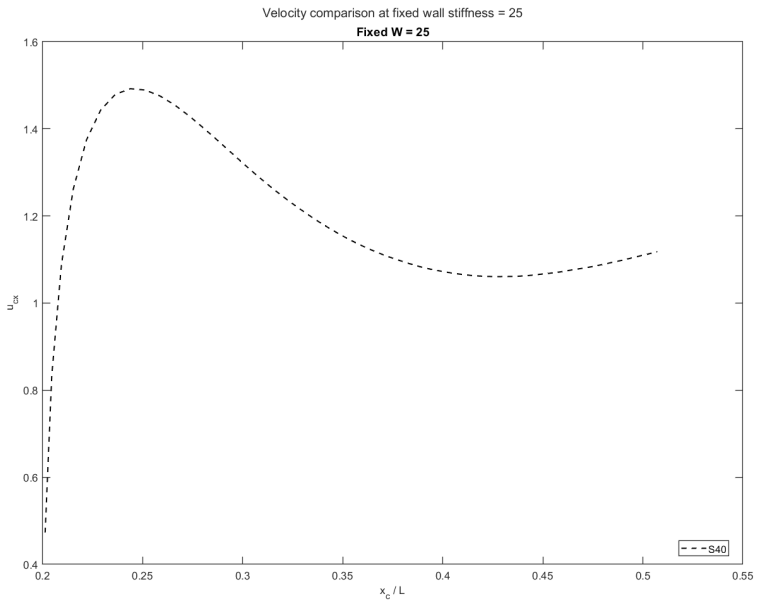

FIG. 8 Velocity comparison at fixed wall stiffness $W = 25$.

In the second set, the different solid stiffness values are compared with walls having an intermediate stiffness equal to $W = 50$, so as to also analyze the transition from soft walls to stiffer confinement. Also in this case, the comparison is carried out among the cases with $S = 20$, $S = 40$, and $S = 80$. A representative comparison for this set is reported in Fig. 9, while the

velocity-only comparison is shown in Fig. 10.

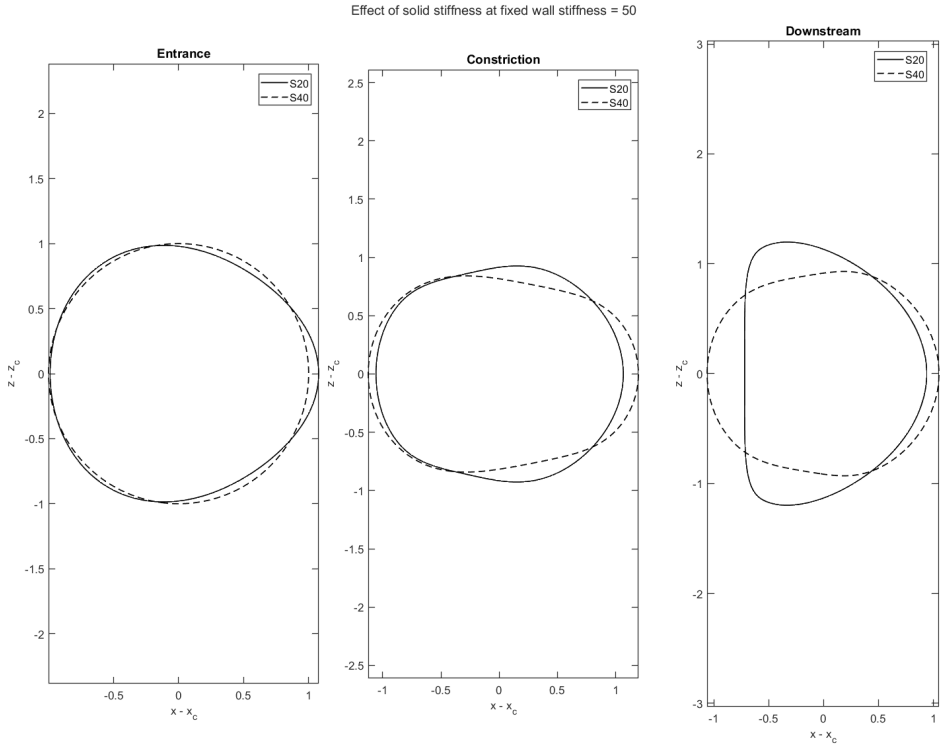

FIG. 9 Effect of the solid stiffness at fixed wall stiffness $W = 50$.

At intermediate wall stiffness, the comparison becomes particularly useful because it shows how the geometric response and the velocity response remain consistent with each other as the stiffness of the solid is varied.

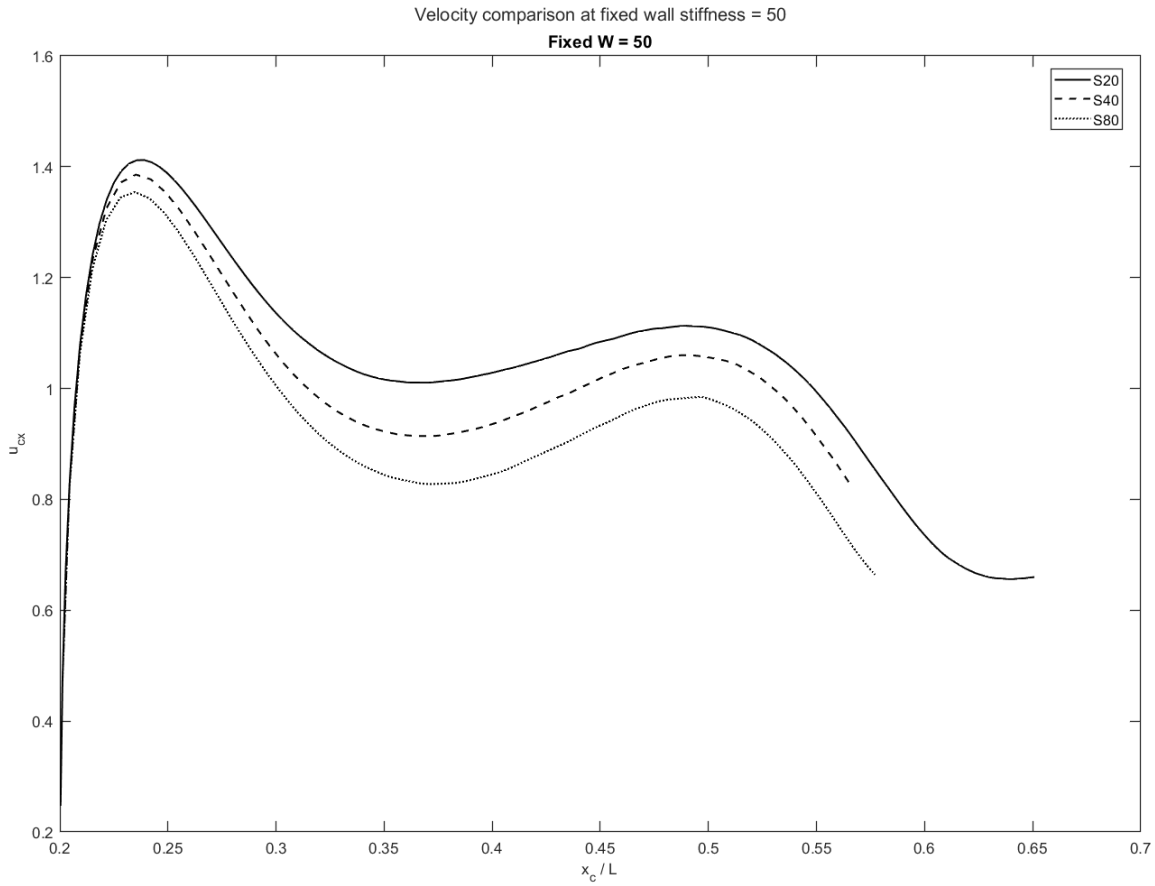

FIG. 10 Velocity comparison at fixed wall stiffness $W = 50$.

Finally, in the third set the comparison is carried out by fixing the wall stiffness at $W = 100$. The results serve to understand whether the solid maintains a robust role even in such a stiff confinement, or whether the behavior of the external confinement prevails. Although the corresponding coupled shape–velocity plot is not available here, the qualitative trend follows the same organization observed for the representative $W = 25$ and $W = 50$ cases.

Overall, as could reasonably be expected, as the stiffness of the solid increases, the deformation tends to decrease and the shape assumed after passing through the constriction tends to be more similar to the initial one. In parallel, the softer solids show a greater ability to adapt to the constriction and a more evident memory of the passage in the final stage. This trend is also reflected in the quantitative velocity comparison at fixed wall stiffness $W = 50$, where the selected cases $W50$-$S20$, $W50$-$S40$, and $W50$-$S80$ show a progressive reduction of the main maximum streamwise velocity from 1.4132 to 1.3858 and then to 1.3545. The same ordering is preserved for the local minimum and for the second downstream maximum, which decrease from 1.0105 to 0.9140 and 0.8275, and from 1.1126 to 1.0600 and 0.9842, respectively. These values indicate that increasing solid stiffness does not only reduce the peak acceleration, but dampens the entire velocity response along the streamwise direction.

5.5 Effect of the wall stiffness at fixed solid stiffness

In this section, the point of view is reversed, keeping the stiffness of the solid constant while varying that of the walls. The reason behind this choice is to understand how the external confinement modifies the response of the body when its internal stiffness remains unchanged. In this case as well, the focus is on the shape of the solid during the various phases. Here, it is reasonable to expect that stiffer walls make the passage more difficult and, consequently, more capable of modifying the shape of the solid, although this remains a hypothesis to be verified.

The first set of cases includes those in which the stiffness of the solid is equal to 20, making the contribution of the solid body the least rigid among the considered cases. The comparison is therefore carried out among the cases with $W = 25$, $W = 50$, and $W = 100$. A representative coupled comparison for this group is shown in Fig. 11.

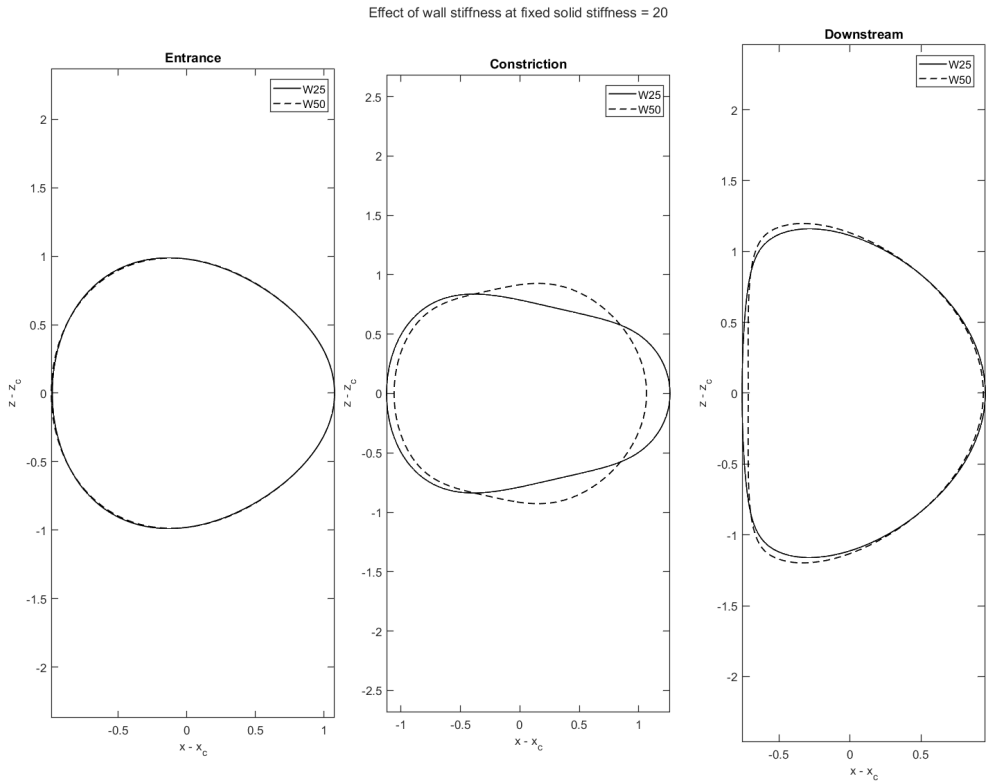

FIG. 11 Effect of the wall stiffness at fixed solid stiffness $S = 20$.

Once the behavior of the softest solid has been outlined, it is useful to move to the intermediate-stiffness case, where the role of wall compliance can be observed under a more balanced solid–wall interaction.

In the second set, the different wall stiffness values are compared while the solid has an intermediate stiffness equal to $S = 40$. A representative comparison for this group is shown in Fig. 12, while the corresponding velocity-only comparison is reported in Fig. 13.

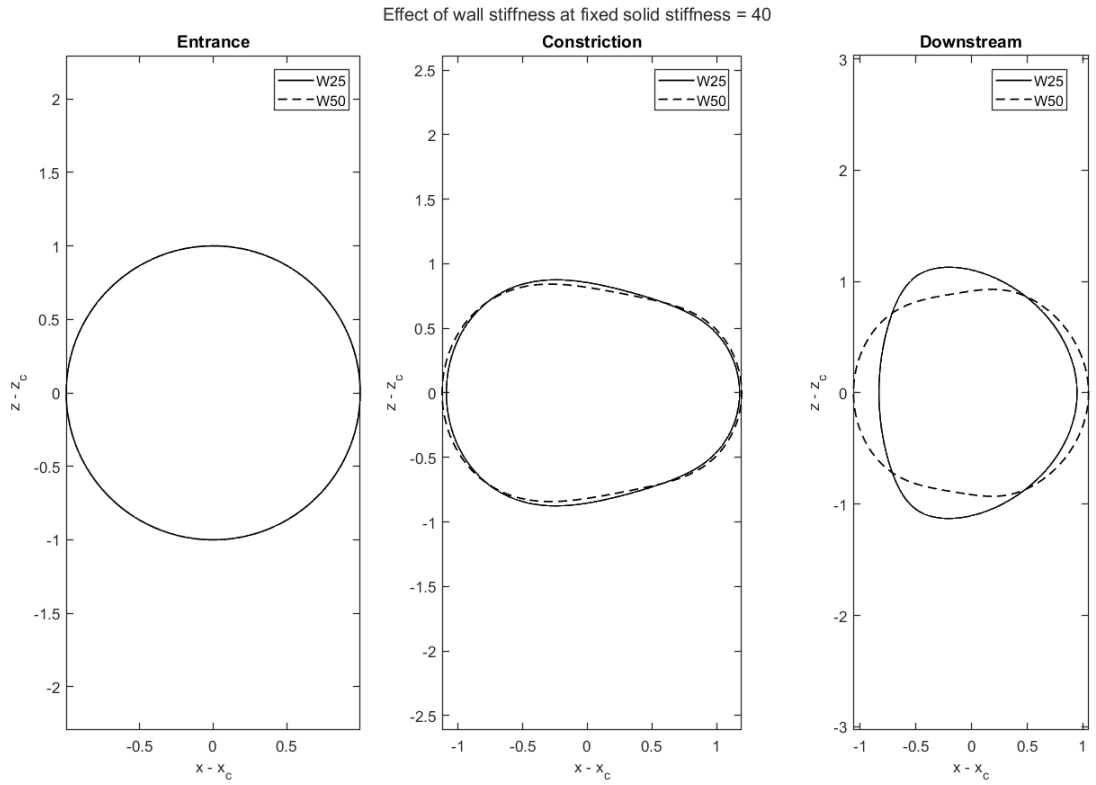

FIG. 12 Effect of the wall stiffness at fixed solid stiffness $S = 40$.

The corresponding velocity comparison complements the geometric picture by showing how the same change in confinement is reflected in the amplitude and modulation of the streamwise centroid response.

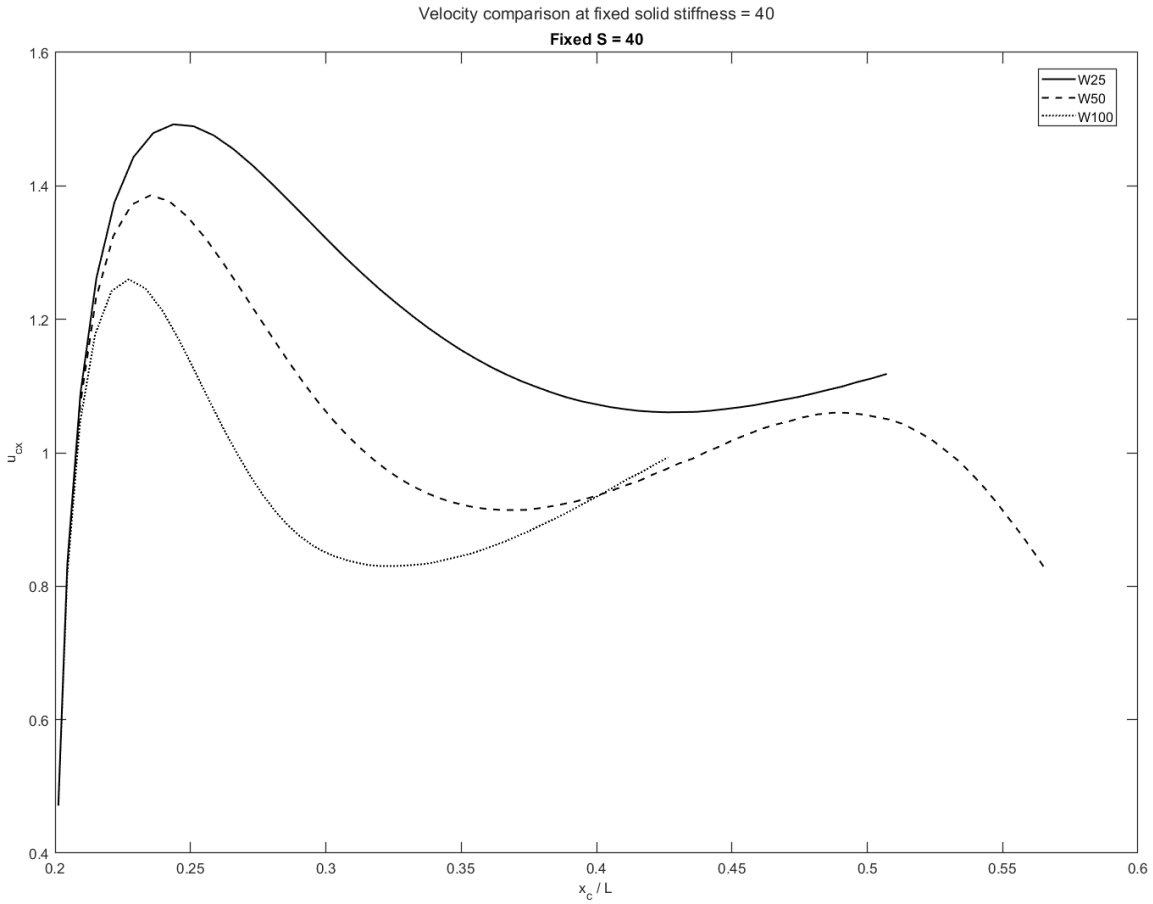

FIG. 13 Velocity comparison at fixed solid stiffness $S = 40$.

Finally, in the third set the comparison is carried out by fixing the stiffness of the solid at $S = 80$. The results serve to understand whether the walls continue to produce appreciable differences or whether the behavior of the system is dominated by the stiffness of the body. The corresponding velocity comparison is shown in Fig. 14.

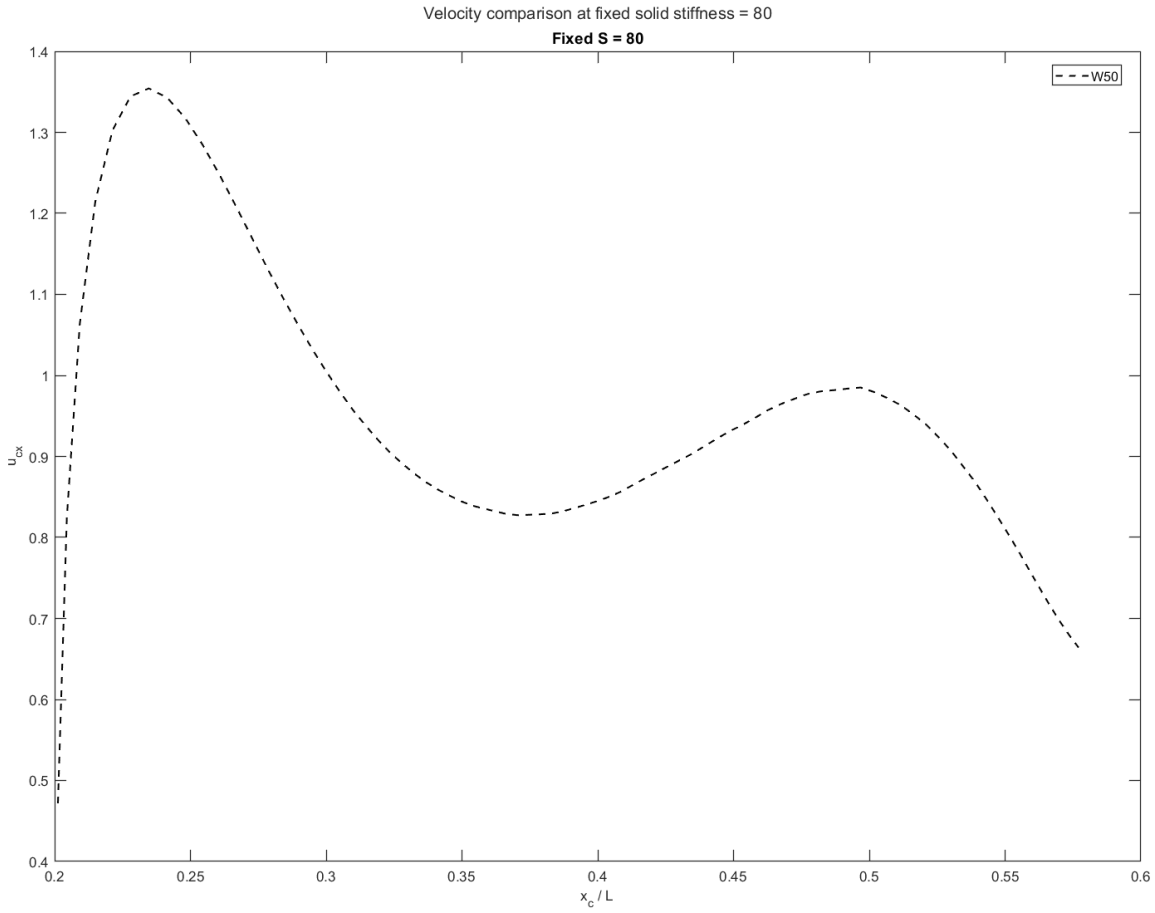

FIG. 14 Velocity comparison at fixed solid stiffness $S = 80$.

To conclude, it is emphasized that the increase in wall stiffness makes the effect of confinement more evident, especially when the solid is more deformable. Softer walls, on the contrary, favor a more regular response and a faster recovery of the shape. This behavior is also confirmed by the quantitative comparison at fixed solid stiffness $S = 40$, where the selected cases $W25$-$S40$, $W50$-$S40$, and $W100$-$S40$ show a systematic reduction of the main maximum velocity from 1.4925 to 1.3858 and then to 1.2592. The local minimum decreases from 1.0607 to 0.9140 and 0.8301, while the second downstream maximum decreases from 1.1181 to 1.0600 and 0.9934. This indicates that increasing wall stiffness compresses the whole velocity profile and makes the downstream relaxation less pronounced.

5.6 Detailed shape evolution in representative cases

It is useful to focus on particularly significant cases. This choice makes it possible to interpret the phases of the phenomenon more accurately by selecting those cases that allow a continuous and clear reading of the studied system. The continuous evolution of the body inside the channel for the representative cases is shown in Fig. 15.

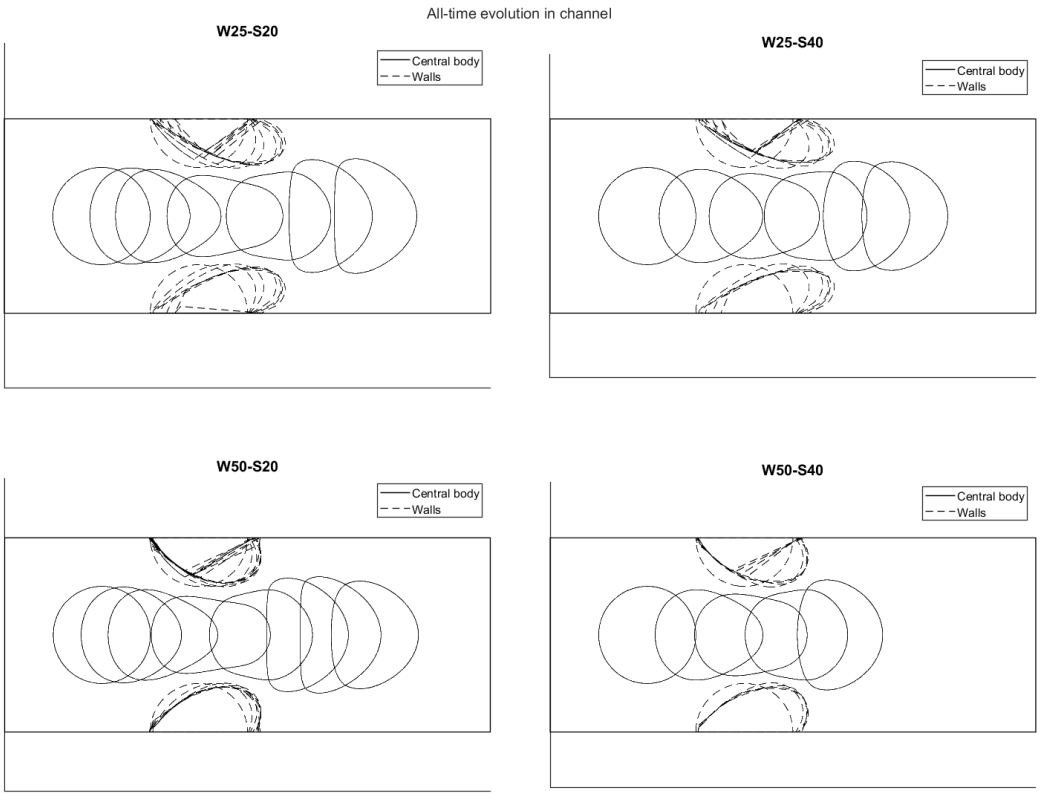

FIG. 15 All-time evolution in the channel for representative cases.

Among the representative cases shown, $W25$-$S20$ is the one in which the solid is most strongly influenced by the presence of the constriction, with a larger departure from the initial configuration. On the contrary, $W50$-$S40$ shows a more regular response, with a smaller overall distortion and a faster tendency toward a downstream recovery. These representative cases are sufficient to show that the passage is not characterized by an abrupt deformation limited to the throat alone, but by a continuous shape evolution that begins upstream of the constriction and persists downstream. This continuous evolution is consistent with the velocity profiles, in which the first maximum appears before the centroid reaches the center of the constriction, indicating that the body starts to react to the converging geometry already in the upstream region.

After considering the continuous evolution of the body throughout the passage, it is useful to isolate the downstream configuration in order to compare more clearly the residual deformation retained by the different cases.

5.7 Morphology of the solid in the final stage of the passage

The final stage deserves a brief discussion because it represents one of the most significant aspects of the entire problem. In all the considered cases, the final configuration does not coincide with the initial one. Once it has reached the downstream region, the solid tends to preserve the deformation acquired during the passage through the constriction, although in a

variable way.

A direct comparison of the final shapes, centered with respect to the centroid, is shown in Fig. 16. This representation isolates the residual morphological differences without the effect of the rigid translation of the body.

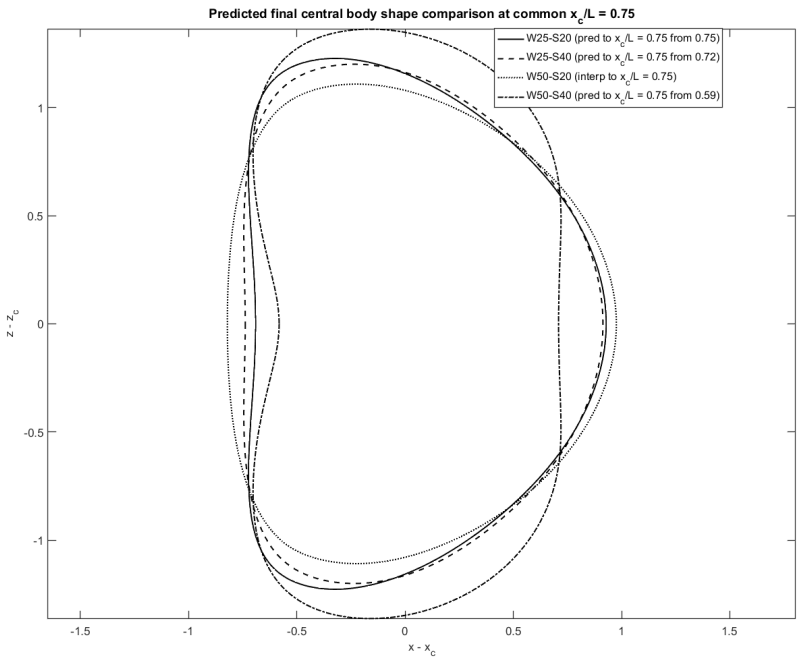

FIG. 16 Comparison of the final centered body shapes.

The comparison confirms that the final stage does not represent only the end of the phenomenon, but rather a physically meaningful phase in which the memory of the passage is still clearly visible. The cases differ not only in the degree of deformation reached inside the constriction, but also in the extent to which this deformation is retained downstream. This clarification is necessary because it confirms that the final stage is highly representative of the possible outcomes of the fluid–structure interaction. This residual deformation is also coherent with the presence of a second local maximum in the streamwise velocity profiles, which can be interpreted as the kinematic signature of the downstream relaxation process.

5.8 Comparison of the streamwise centroid velocity

In this section, the velocity of the centroid of the immersed solid is analyzed because it constitutes the most effective quantitative measure for describing the global transport dynamics. Attention is focused on the component of this velocity in the direction of motion, which makes it possible to interpret how the stiffness of both the solid and the constriction influences the crossing of the constriction itself. The representation of the velocity along the streamwise coordinate relates the kinematics of the body to the different phases of the phenomenon, consistently with the work previously carried out.

Before analyzing the profiles, it is necessary to clarify the geometric configuration of the

system. The two constrictions are fixed and centered at the position $x = 4$, placed symmetrically with respect to the channel centerline at $z = 0$ and $z = 4$. The deformable solid, on the other hand, starts from the initial position $(x, z) = (2, 2)$. Consequently, it is possible to distinguish the different phases of the motion: for $x_c < 4$ the body is upstream of the constriction, at $x_c = 4$ it is in the constriction region, and for larger values it is in the exit phase, followed by the downstream relaxation phase. It should be remembered that the body has a finite size, and therefore it begins to be affected by the constriction before its centroid reaches the geometric center of the narrowing.

By observing all the available profiles, it is possible to notice a similar behavior in all cases. In the initial phase, starting from lower values before entering the confined region, the velocity increases rapidly until it reaches a main maximum before the constriction, and then decreases. In other words, this first maximum is associated with the approach of the solid to the entrance of the constriction, rather than with its complete passage through it. The dynamics are therefore interpreted along the trajectory, highlighting the asymmetry between the approach phase and the exit phase from the constriction.

Representative comparisons of the streamwise centroid velocity at fixed wall and solid stiffness are reported in Figs. 8, 10, 13, and 14. These comparisons show that the overall structure of the velocity profile is preserved across the different cases, while the amplitude of the maxima, the depth of the intermediate minimum, and the persistence of the downstream modulation vary according to the relative stiffness of the solid and the walls. The quantitative comparison of the selected cases confirms this point more clearly: the main maximum ranges from 1.4925 in $W25$-$S40$ to 1.2592 in $W100$-$S40$, while at fixed $W = 50$ it decreases from 1.4132 in $W50$-$S20$ to 1.3545 in $W50$-$S80$.

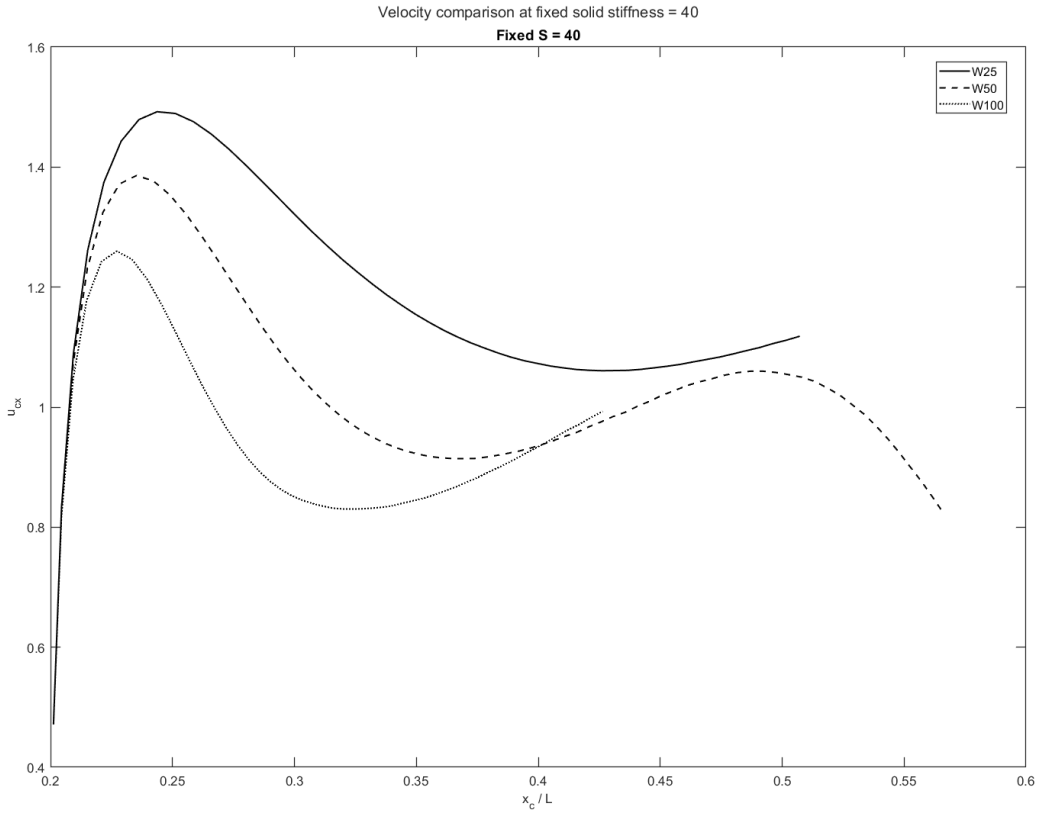

FIG. 17 Streamwise velocity at fixed solid stiffness $S = 40$.

A complementary reading is obtained by reversing the comparison criterion, so as to assess whether the same profile structure is preserved when wall stiffness, rather than solid stiffness, is varied.

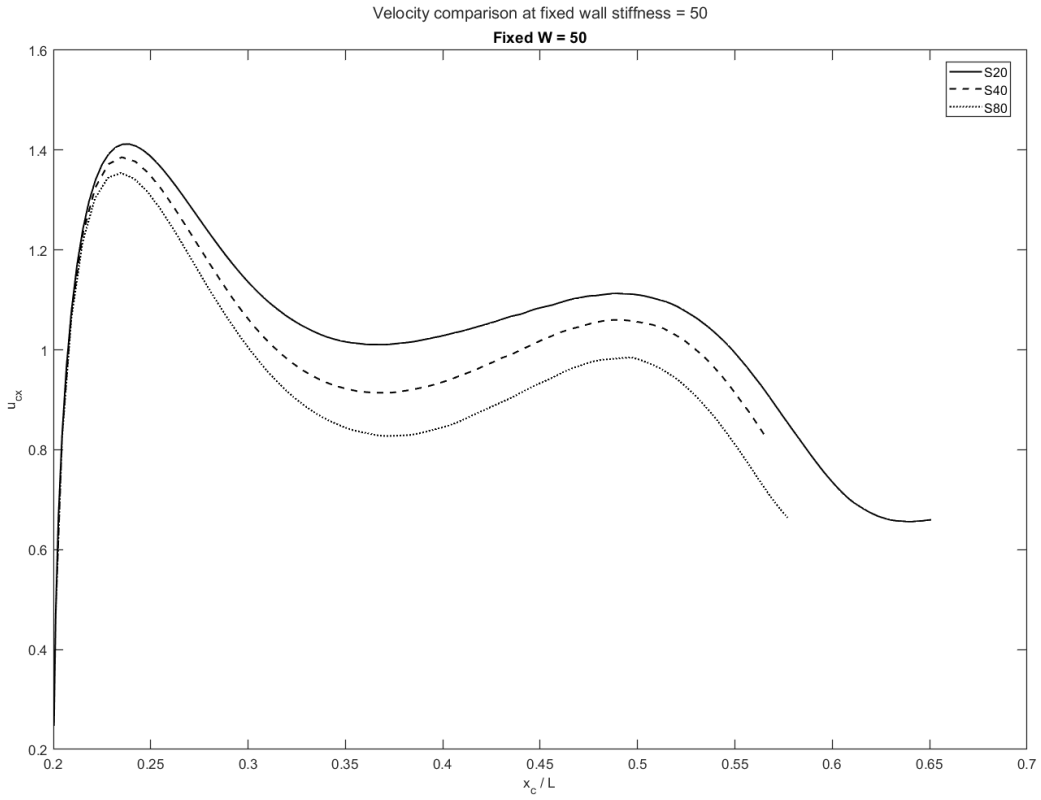

FIG. 18 Streamwise velocity at fixed wall stiffness $W = 50$.

However, this decrease is not monotonic up to complete stabilization. An intermediate phase can be observed, in which the initial decay gives way to a smoother variation, readable as a second local maximum, before the final downstream readjustment. This decrease is due to the dynamic reorganization of the system in the region of maximum confinement. In this region, the body is modifying its shape in order to adapt to the constriction, and for this reason the streamwise velocity is lower.

It is also possible to observe the presence of a second local maximum just as the solid is about to leave the constriction. This variation can be interpreted as a signature of the relaxation phase, since the solid still retains a mechanical memory of the passage. This observation is consistent with the literature, where great importance is attributed to the downstream part of the profiles precisely to identify the delay in the relaxation of the solid.

To make the interpretation of these profiles more explicit, it is useful to consider a single representative case in which the three characteristic stages of the streamwise velocity evolution can be identified directly.

A representative smooth profile, in which the first maximum, the intermediate minimum, and the second downstream maximum are explicitly identified, is shown in Fig. 19.

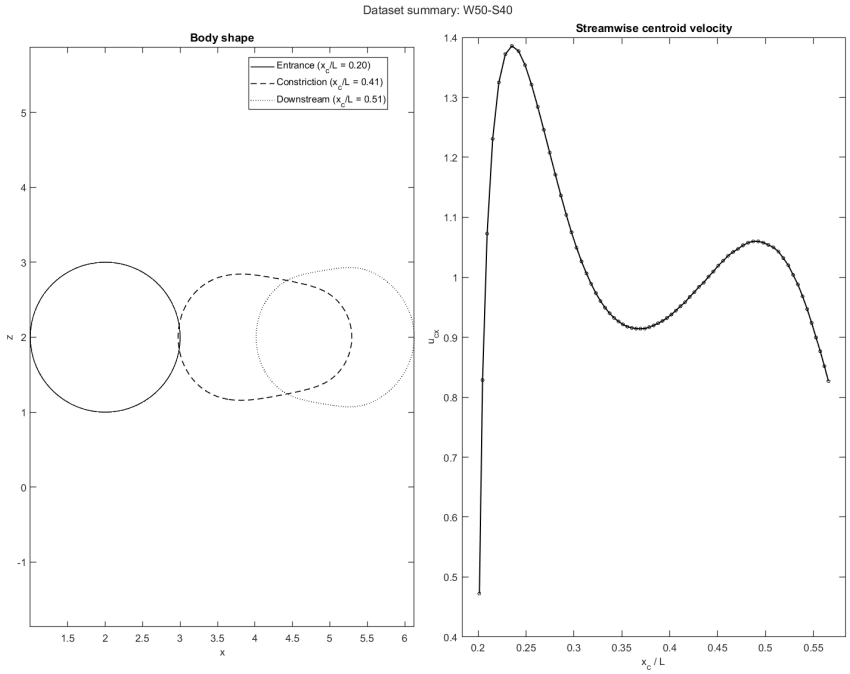

FIG. 19 Smooth streamwise centroid velocity profile for the representative case $W50$-$S40$.

Turning to the comparison at fixed wall stiffness, it emerges that when the walls are more compliant, with $W = 25$, the case with the lowest solid stiffness is the one showing the highest velocity profile. The initial growth is more pronounced, the first maximum reaches a higher value, and the subsequent evolution preserves the memory of the passage more clearly. As the stiffness of the solid increases, the profile progressively lowers, and the response in the final phase also tends to become more damped. This is due to the fact that a softer body is able to adapt better to the converging flow region and is therefore accelerated more intensely, whereas a stiffer body offers greater resistance. The same trend is quantitatively documented for the cases with $W = 50$, where the ordered sequence $W50$-$S20$, $W50$-$S40$, and $W50$-$S80$ shows not only decreasing peak values but also a progressive reduction of the minimum and of the second downstream maximum. From this perspective, the stiffness of the solid does not govern only the maximum value of the velocity, but the entire structure of the profile along the streamwise axis.

Similarly to what was stated above, at fixed solid stiffness, the cases characterized by greater wall compliance also show higher velocities, especially in the phase preceding and accompanying the entrance into the constriction. On the contrary, as the wall stiffness increases, the profile lowers and appears overall more compressed. This suggests that stiffer walls make the confinement less accommodating and transfer a larger part of the response into the deformation of the system, reducing the streamwise component of the centroid velocity. This is particularly clear for $S = 40$, where moving from $W25$-$S40$ to $W50$-$S40$ and then to $W100$-$S40$ leads to a systematic decrease of all three characteristic extrema of the profile.

Table 5.1: Characteristic extrema of the streamwise centroid velocity for the selected cases.

Case	Max $u_{c,x}$	First local min $u_{c,x}$	Second max after first min $u_{c,x}$
W100-S40	1.2592	0.8301	0.9934
W25-S40	1.4925	1.0607	1.1181
W50-S20	1.4132	1.0105	1.1126
W50-S40	1.3858	0.9140	1.0600
W50-S80	1.3545	0.8275	0.9842

Overall, the analysis of the streamwise centroid velocity confirms that the passage of the solid through the constriction can be divided into three well-defined phases: an acceleration phase upstream of the narrowing, a crossing phase through the throat centered around $x = 4$, and a downstream relaxation phase characterized by a response that is still active and not immediately exhausted.

5.9 Perimeter and axis ratio at the center of the constriction

From the point of view of deformation, two additional geometric indicators are considered when the particle is located at the center of the constriction: the perimeter of the contour and the ratio between the major and minor axes, calculated as the ratio between the dimension in the streamwise direction and that in the normal direction. These two quantities make it possible to describe more clearly and effectively the shape of the body in the region of maximum confinement, where the interaction with the channel geometry is stronger.

Table 5.2: Perimeter and streamwise-to-normal axis ratio of the solid at the center of the constriction.

Case	Perimeter	Axis ratio ($a_{\text{str}}/a_{\text{norm}}$)
W25-S20	6.5501	1.4235
W25-S40	6.3215	1.1558
W50-S20	6.6142	1.5426
W50-S40	6.4538	1.3772

As shown in the table, the obtained values highlight clear differences among the analyzed cases. The case $W25$-$S20$ presents a perimeter equal to 6.5501 and an axis ratio equal to 1.4235. In the case $W25$-$S40$, with the same wall stiffness but a stiffer solid, both values decrease, with a perimeter of 6.3215 and an axis ratio of 1.1558, indicating a less elongated and overall less deformed shape. A similar behavior is also observed for the pair of cases with stiffer walls. Indeed, $W50$-$S20$ shows the highest value of both the perimeter, equal to 6.6142, and the ratio between the major and minor axes, equal to 1.5426, whereas $W50$-$S40$ presents lower values, namely 6.4538 and 1.3772, respectively.

Overall, the comparison shows that, at fixed wall stiffness, the cases with a less stiff solid lead to a more pronounced deformation than the corresponding cases with a stiffer solid, both in terms of contour extension and in terms of elongation of the shape along the flow direction. This

aspect is evident when comparing $W25$-$S20$ with $W25$-$S40$ and, in a completely analogous way, $W50$-$S20$ with $W50$-$S40$.

The role of the walls is also appreciable. By comparing cases at fixed solid stiffness, it can be observed that the configurations with stiffer walls tend to produce higher values of perimeter and axis ratio than the corresponding cases with less stiff walls. This suggests that a greater wall stiffening intensifies the confinement effect on the solid in the central region of the constriction, promoting a more pronounced deformation.

Among all the considered cases, $W50$-$S20$ is therefore the most deformed one, whereas $W25$-$S40$ is the one that maintains the most compact shape. Overall, these results confirm that the center of the constriction represents a particularly significant configuration for comparing the combined effect of solid and wall stiffness, since it is precisely in this region that the geometric differences emerge most clearly.

5.10 Coupled interpretation of shape and streamwise velocity

The shape of the solid and the streamwise velocity of its centroid are not two independent observables, but are complementary in revealing the fluid–structure interaction in the presence of deformable confinement. The shape of the body makes its adaptation to the available space visible, whereas the velocity quantitatively translates this adaptation. By analyzing the continuous evolution of the body within the domain, it is clearly observed that the shape is not preserved unchanged up to the center of the constriction and then modified suddenly; rather, this deformation begins before the centroid reaches the center of the constriction. The first maximum of the velocity appears when the body starts to be affected by the converging flow and by the reduction of the available space. The physical link between these two aspects is that the more deformable the body is, the more favorably it can localize itself through the constriction, allowing its centroid to be transported more effectively. This behavior is much less pronounced in the cases with a solid characterized by higher stiffness.

The interdependence between the body configuration and the velocity profile becomes even more significant in the vicinity of the constriction. In this phase, the solid reorganizes itself, leading to a decrease in the velocity profile. Downstream of the constriction, this coupled behavior remains evident: the body does not immediately recover its initial configuration, but retains a residual deformation that remains clearly recognizable along the downstream tract. Consistently, the centroid velocity also does not immediately stabilize to a uniform trend, but instead exhibits a secondary modulation, broader and less intense than the first maximum. The comparison among the cases therefore shows that the greater or lesser intensity of the kinematic response does not constitute information separate from the deformation of the body, but rather represents its dynamic counterpart. From this perspective, the joint reading of shape and velocity makes it possible to interpret the passage of the body through the constriction as a unitary phenomenon, governed by the distribution of deformability between the solid and the confinement. The quantitative indicators support this same interpretation: the cases that show

larger perimeter and axis-ratio values at the center of the constriction are also associated with stronger streamwise modulation, whereas the configurations with more compact shapes exhibit a more damped velocity response.

Chapter 6

Conclusions

The present work analyzed the passage of a deformable solid through a confined region bounded by deformable walls, with the aim of clarifying how the distribution of stiffness between the body and the confinement influences the deformation of the solid and the dynamics of its transport. The analysis was carried out through a parametric study based on the combination of different values of solid and wall stiffness, while keeping the other problem parameters constant.

In conclusion, the initial questions of the work find a clear answer. The passage of the body through the constriction is directly influenced by both the stiffness of the solid and that of the walls; the final phase of motion retains a significant memory of the interaction just experienced; and the centroid velocity, considered together with the evolution of shape, constitutes an effective tool for interpreting the phenomenon in a unified way.

6.1 Limitations of the work

It is necessary to take note of some limitations in the interpretation of the results of this work. First, the analysis was conducted in a two-dimensional context, which makes it possible to clearly capture the main mechanisms of the problem but does not reproduce the full complexity of a real three-dimensional configuration. In a three-dimensional geometry, additional effects could in fact emerge, related to the curvature of the body, the spatial distribution of stresses, and the possible presence of out-of-plane dynamics.

A second limitation concerns the number and extent of the cases considered. The parametric study was constructed on a selected set of values of solid and wall stiffness, sufficient to highlight the main trends but not yet extensive enough to provide an exhaustive mapping of the parameter space. Consequently, the results obtained should be interpreted as a coherent description of the trends observed within the studied range, rather than as a universal generalization.

The problem was analyzed by considering a single deformable body, without including interactions among multiple particles or collective effects. In the presence of multiple bodies, the passage dynamics could be significantly different because of mutual interactions and possible phenomena of accumulation, shielding, or cooperation in the confined region[16].

Finally, the adopted model is based on the constitutive and numerical assumptions defined in the previous chapters. Although these assumptions are appropriate for the objectives of the work, the introduction of different constitutive models or more complex boundary conditions could quantitatively modify some results, without necessarily altering the general qualitative picture that emerged.

6.2 Future developments

Starting from the results obtained, several future developments can be identified. A first continuation of the work could extend the analysis to three-dimensional configurations, in order to verify to what extent the mechanisms observed in two dimensions remain valid also in a more realistic context.

Another possible development concerns the expansion of the parametric study. It would be useful to consider a larger number of combinations of solid and wall stiffness, in order to build a more systematic classification of the response regimes and identify more precisely the thresholds between different behaviors.

A further step consists in introducing multiple deformable bodies within the domain, in order to study collective effects, hydrodynamic interactions, and possible modifications of transport due to the simultaneous presence of multiple particles in the confined region. This type of extension would make the model closer to situations of applied interest.

From a geometric point of view, it would be interesting to analyze constrictions with different shapes or channels with asymmetric confinement, in order to assess the role of geometry in determining the deformation, trajectory, and downstream relaxation of the body. As regards the solid, it might not be circular, or spherical if analyzed in a three-dimensional context, but instead have different and more complex shapes.

Finally, from a numerical point of view, strategies may be developed to reduce the computational cost, improve the resolution of the most delicate phases of passage through the constriction, and make the exploration of wider parametric spaces more efficient.

Bibliography

[1] Pedro Costa. A fft-based finite-difference solver for massively-parallel direct numerical simulations of turbulent flows. *Computers & Mathematics with Applications*, 76(8):1853–1862, 2018.

[2] Florian Desmons, Thomas Milcent, Anne-Virginie Salsac, and Mirco Ciallella. Fully Eulerian models for the numerical simulation of capsules with an elastic bulk nucleus. *Journal of Fluids and Structures*, 127:104109, 2024.

[3] Rafael Diez Sanhueza, Jurriaan Peeters, and Pedro Costa. A pencil-distributed finite-difference solver for extreme-scale calculations of turbulent wall flows at high reynolds number. *Computer Physics Communications*, 316:109811, 2025.

[4] Tong Gao and Howard H. Hu. Deformation of elastic particles in viscous shear flow. *Journal of Computational Physics*, 228:2132–2151, 2009.

[5] Dongwoo Han, Alexander Starikov, Bríain Ó Hartaigh, Heidi Gransar, Kiran K. Kolli, Joon-Hyung Lee, Arbab Z. Rizvi, Lakshmanan Baskaran, Fay Y. Lin, Byoung Kwon Choi, Jongmin Sung, Jeffrey P. Earls, Philipp Blanke, Martin Hadamitzky, Jörg Hausleiter, Mouaz H. Al-Mallah, Matthew J. Budoff, Daniel S. Berman, and James K. Min. Relationship between endothelial wall shear stress and high-risk atherosclerotic plaque characteristics for identification of coronary lesions that cause ischemia: A direct comparison with fractional flow reserve. *Journal of the American Heart Association*, 5(12):e004186, 2016.

[6] Suhas S. Jain, Ken Kamrin, and Ali Mani. A conservative and non-dissipative eulerian formulation for the simulation of soft solids in fluids. *Journal of Computational Physics*, 399:108922, 2019.

[7] Ken Kamrin, Chris H. Rycroft, and Jean-Christophe Nave. Reference map technique for finite-strain elasticity and fluid–solid interaction. *Journal of the Mechanics and Physics of Solids*, 60(11):1952–1969, 2012.

[8] Stéphane Popinet. Numerical models of surface tension. *Annual Review of Fluid Mechanics*, 50:49–75, 2018.

[9] Cecilia Rorai, Antoine Touchard, Lailai Zhu, and Luca Brandt. Motion of an elastic capsule in a constricted microchannel. *The European Physical Journal E*, 38:49, 2015.

[10] Marco E. Rosti and Luca Brandt. Numerical simulation of turbulent channel flow over a viscous hyper-elastic wall. *Journal of Fluid Mechanics*, 830:708–735, 2017.

[11] Marco Edoardo Rosti, Mehdi Niazi Ardekani, and Luca Brandt. The effect of elastic walls on suspension flow, June 2019. arXiv preprint.

[12] Chris H. Rycroft, Chen-Hung Wu, Yue Yu, and Ken Kamrin. Reference map technique for incompressible fluid–structure interaction. *Journal of Fluid Mechanics*, 898:A9, 2020.

[13] Zubeir Allum Saib, Farid Abed, Mergen H. Ghayesh, and Marco Amabili. A review of fluid-structure interaction: blood flow in arteries. *Biomechanics and Applications*, 3:100171, 2025.

[14] Kiran Satheeshchandran, Salar Zamani Salimi, Lisa Prahl Wittberg, and Luca Brandt. An Eulerian diffuse-interface method for simulation of elastic capsules in flow, January 2025. SSRN working paper.

[15] Kazuyasu Sugiyama, Satoshi Ii, Shintaro Takeuchi, Shu Takagi, and Yoichiro Matsumoto. A full Eulerian finite difference approach for solving fluid–structure coupling problems. *Journal of Computational Physics*, 230:596–627, 2011.

[16] Boris Valkov, Chris H. Rycroft, and Ken Kamrin. Eulerian method for multiphase interactions of soft solid bodies in fluids. *Journal of Applied Mechanics*, 82(4):041011, 2015.